Quantitative seismic characterization of CO_2 at the Sleipner storage site, North Sea

Bastien Dupuy[1], Anouar Romdhane[1], Peder Eliasson[1], Etor Querendez[1], Hong Yan[2], Verónica A. Torres[2], and Amir Ghaderi[1]

Abstract

Reliable quantification of carbon dioxide (CO_2) properties and saturation is crucial in the monitoring of CO_2 underground storage projects. We have focused on quantitative seismic characterization of CO_2 at the Sleipner storage pilot site. We evaluate a methodology combining high-resolution seismic waveform tomography, with uncertainty quantification and rock physics inversion. We use full-waveform inversion (FWI) to provide high-resolution estimates of P-wave velocity V_P and perform an evaluation of the reliability of the derived model based on posterior covariance matrix analysis. To get realistic estimates of CO_2 saturation, we implement advanced rock physics models taking into account effective fluid phase theory and patchy saturation. We determine through sensitivity tests that the estimation of CO_2 saturation is possible even when using only the P-wave velocity as input. After a characterization of rock frame properties based on log data prior to the CO_2 injection at Sleipner, we apply our two-step methodology. The FWI result provides clear indications of the injected CO_2 plume being observed as low-velocity zones corresponding to thin CO_2 filled layers. Several tests, varying the rock physics model and CO_2 properties, are then performed to estimate CO_2 saturation. The results suggest saturations reaching 30%–35% in the thin sand layers and up to 75% when patchy mixing is considered. We have carried out a joint estimation of saturation with distribution type and, even if the inversion is not well-constrained due to limited input data, we conclude that the CO_2 has an intermediate pattern between uniform and patchy mixing, which leads to saturation levels of approximately 25% ± 15%. It is worth noting that the 2D section used in this work is located 533 m east of the injection point. We also conclude that the joint estimation of CO_2 properties with saturation is not crucial and consequently that knowing the pressure and temperature state of the reservoir does not prevent reliable estimation of CO_2 saturation.

Introduction

In the North Sea, an industrial-scale CO_2 storage pilot site has been in operation since 1996. The CO_2 separated from the produced natural gas in the Sleipner West field is being stored at approximately 1000 m depth into a relatively thick reservoir unit, the Utsira Formation, with an approximate injection rate of 0.9 million tons per year. To monitor the CO_2 plume development in the reservoir and the cap rock integrity, a geophysical monitoring program including seismic, seabed, gravimetric, and electromagnetic surveys has been conducted. The extensive monitoring program offered great possibilities to evaluate strategies for monitoring the CO_2 migration and early detection of eventual leakages through the overburden.

Time-lapse seismic analysis has been the main focus to qualitatively map the CO_2 migration process (Arts et al., 2004; Chadwick et al., 2010). Eight repeated surface seismic surveys have been acquired by 2014 at the

Sleipner field. Seismic interpretation and reservoir characterization (Arts et al., 2004; Furre and Eiken, 2014) provided valuable information about the geometry and the lateral extent of the developing CO_2 plume. The studies showed that the CO_2 accumulates in thin sandstone layers, below thinner and mostly impermeable shale beds. Various methods have been used to estimate the thickness of the CO_2-bearing layers. These include structural mapping (Williams and Chadwick, 2012), estimates from seismic frequency decomposition (White et al., 2013), seismic modeling of thin-layer response (Ghaderi and Landrø, 2009), and analysis with respect to time shifts developments and amplitudes changes using full-fold stacked data (Chadwick et al., 2005; Furre et al., 2015). Amplitude variation with offset (AVO) analysis has also been attempted at Sleipner given its higher sensitivity to the presence and level of saturation variation of CO_2 (Brown et al., 2007).

In Sleipner data, the reflected events are strong and easily identified (Arts et al., 2004), but it has been shown that the interpretation is not straightforward due to tuning effects related to thin-layer interferences (Brown et al., 2007; Buddensiek et al., 2010; Ravazzoli and Gómez, 2014). Ghaderi and Landrø (2009) develop an analytical technique for simultaneous inversion of thickness and velocity of a brine-CO_2 partially saturated thin layer based on measured traveltime shifts and 4D amplitude changes. They study time-lapse effects in the prestack domain at Sleipner to derive, simultaneously, velocity and thickness changes due to CO_2 injection. Buddensiek et al. (2010) apply the advanced AVO methodology developed by Causse et al. (2007), to analyze the top-most reflection from a series of thin-layer reflections at Sleipner. Ghosh et al. (2015) estimate CO_2 saturation from poststack seismic impedance considering dual porosity and a pressure-dependent differential effective medium model.

One of the most important challenges at Sleipner is the proper understanding of saturation development during CO_2 injection. The effective seismic velocity of the brine-CO_2 mixture is indeed highly uncertain, and it is dependent on the saturation distribution. The reservoir unit is 800–1100 m deep, with pressure and temperature conditions very close to the supercritical point for CO_2. Small changes in temperature and pressure conditions can therefore result in significant CO_2 property changes, which lead to large velocity and density changes. In addition, geologic characterization of the sandy Utsira Formation shows the presence of thin mudstone beds, with thicknesses ranging from less than 1 up to 3 m (Zweigel et al., 2004). These thin layers partially trap the rising CO_2 (due to buoyancy effects) toward the thick mudstone caprock above the reservoir. Analysis of velocity contrasts between these thin mudstone layers and the CO_2-bearing sand layers suggests the presence of complex effects including thin bed tuning, apparent seismic attenuation, and interbed multiples. The detailed subseismic geologic features strongly affect the in situ CO_2 distribution and contribute to uncertainties in any prediction.

Another source of uncertainty when trying to quantify CO_2 saturation is related to the use of relevant rock physics models. Proper rock physics approaches have to be used to derive CO_2 saturation with more confidence. Mohapatra et al. (2012) conduct laboratory experiments on partially saturated sandstone (gas-brine, oil-brine, and CO_2-brine) and show that the P-wave velocities and impedances are in good agreement with laboratory measurements except for liquid CO_2 flooding. Usually, Gassmann fluid substitution (Gassmann, 1951) combined with effective fluid bulk modulus (calculated by averages) are used for estimation of saturation from seismic velocities or time shifts (Bergmann and Chadwick, 2015). Otherwise, the Gassmann equation is a zero-frequency approximation and the computation of the effective fluid bulk modulus strongly depends on saturation distribution. In addition, it has been shown recently that wave-induced fluid flows (WIFF) in porous media can be the cause of strong attenuation and dispersion of seismic waves even at low frequencies (Muller et al., 2010). WIFF are especially created in case of patchy saturation, which is likely to occur in a highly permeable and porous brine-saturated sandstone in which supercritical CO_2 is injected (Rubino et al., 2011). Using average mixing theories (patchy or uniform) is not enough because this comes down to calculate an average fluid modulus and use it as input to the Gassmann equation. Using WIFF theory to account for complex pressure gradient equilibrations in fluid phases (Pride et al., 2004) allows considering physical mechanism-based relations between seismic properties (velocities and quality factors versus frequency) and saturation and other poroelastic properties.

Given the inherent difficulties in the estimation of CO_2 saturation with amplitude-based methods, an alternative approach consists of using full-waveform inversion (FWI), which is a high-resolution tomographic method. By exploiting all information contained in the seismic signal, the method has the highest potential in terms of resolution to locate and provide quantitative estimates of velocity changes caused by the presence of injected CO_2. At Sleipner, attempts to derive high-resolution quantitative maps of velocity properties have been made (Queißer and Singh, 2013; Romdhane and Querendez, 2014; Raknes et al., 2015). Although the method can locate and image the CO_2 plume, seen as property changes induced by the CO_2 injection, the quantification of the uncertainty in the reconstructed parameters is challenging. Global uncertainty quantification of the full model space represents a computational burden, which can be solved by coarsening the model grid sampling for global search methods (Fernádez-Martínez et al. 2013), or by dimension reduction using principal component analysis (Fernádez-Martínez, 2015), to provide coarse approximation of the global uncertainty. A more realistic approach, based on the posterior covariance matrix analysis (Tarantola, 2005), estimates uncertainty of the reconstructed parameters locally, assuming that the obtained model vector is close to the global optimum. Examples of applications of this approach for tomographic methods are discussed by Duffet and Sinoquet (2006), Fichtner and Trampert (2011), Zhu et al. (2016), and Eliasson and Romdhane (2017).

In this paper, we aim at giving principles and first examples for reliable quantification of CO_2 saturation based on seismic monitoring methods. Introducing advanced rock physics models, we will assess the possibility of quantitative estimation of CO_2 saturation and associated uncertainties. We will give examples of quantitative seismic imaging based on the analysis of the full seismograms together with an estimation of the local uncertainties of these results. Finally, rock physics inversion of CO_2 saturation will be developed, taking into account various rock physics models and input properties. We will show sensitivity tests and field data application.

Geologic setting and rock physics models
### Geology overview

The Utsira sands is a saline reservoir beneath the central and northern North Sea, which is covering an area of more than 2.6×10^4 km^2. The pore volume is estimated to 5.5×10^{11} m^3 and combined with its regional extent, it makes the formation suitable for large-scale storage of CO_2. The Utsira Formation is composed of basinally restricted Miocene to Pliocene, mainly uncemented sand deposits pinching out toward east and west. The grain sizes are varying from predominantly coarser to finer toward south. Northward, the Utsira sands presents complex depositional patterns, with some isolated depocenters and areas of nondeposition within the main depocenter. The top of the formation varies smoothly in a depth range between 700 and 1000 m, and in the Sleipner region, between 800 and 850 m, whereas the base is strongly affected by mud diapirism. The internal structure of the reservoir unit, as interpreted from geophysical log observations, shows intrareservoir 1–2 m thick shale layers, as well as a 5–6 m thick shale layer separating the main Utsira sands body from an overlying eastward thickening sand wedge (the Utsira sands wedge; see Figure 1). The porosity of the Utsira sands from log measurement ranges from 35% to 40%, whereas permeability from core testing ranges between 1 and 3 darcy and up to 8 darcy as estimated from water production testing (Chadwick et al., 2004b; Zweigel et al., 2004). The several hundred meters thick caprock succession above the sand wedge comprises prograding deltaic wedges of Pliocene age overlain by Pleistocene deposits. This succession can be organized into three distinct units (Nordland shales): (1) the Lower Seal composed of mainly shaly deposits, (2) the Middle Seal, with deposits ranging from shaly to sandy toward the basin margin and upward, (3) the Quaternary Upper Seal mainly composed of clays and tills (Chadwick et al., 2004b).

Rock physics models

The rock physics models used in this work are built from Biot-Gassmann theories (Gassmann, 1951; Biot, 1956a, 1956b). Two approaches are considered for the partial saturation in brine and supercritical CO_2: (1) computing an effective fluid phase with different average techniques, which is used as "one fluid phase" as input into the Biot theory for saturated porous media and (2) patchy saturation taking into account the WIFF mechanisms at mesoscopic scale (Pride et al., 2004; Muller et al., 2010). In both cases, the porous medium is described at the microscopic scale by a set of properties for each solid and fluid phase. The details of rock physics models are given in Appendix A.

Rock physics properties are defined for the Nordland shale caprock and Utsira sands reservoir. Effective grain properties given in Table 1 for shale and sand formations are computed using Hashin-Shtrikman bounds (Hashin and Shtrikman, 1963). Effective grains properties are combining seven different minerals for the Utsira sandstone (mainly quartz and feldspar, see Chadwick et al., 2004b) and 11 minerals for Nordland shales (illite, quartz, kaolinite, and plagioclase having the biggest mass percentages, see Bøe and Zweigel, 2001; Gaus et al., 2005). The brine and CO_2 fluid phase properties in the Utsira sands (see Table 2) are calculated using equation of state (Span and Wagner, 1996). The supercritical CO_2 phase properties are strongly affected by pressure and temperature state, which are ranging between 8 and 11 MPa and between 27°C and 37°C in the reservoir (Ghaderi and Landrø, 2009). For the Utsira sands, we use average values for rock frame properties (Table 3), based on effective fluid phase and patchy saturation theories to compute the viscoacoustic properties for various brine saturations.

Figure 2a shows the P-wave velocity V_P variations versus brine saturation S_w for the effective fluid phase
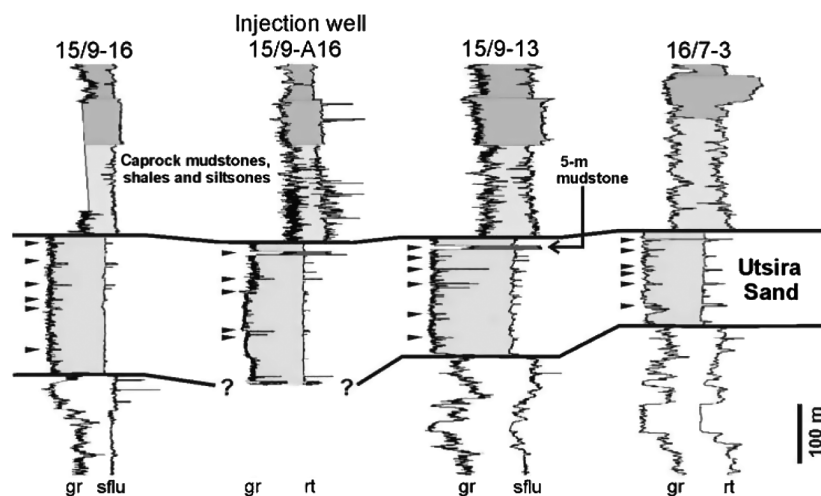
Figure 1. Well correlation panel for the Sleipner area. The geophysical wireline logs for the four wells clearly show the presence of intrareservoir shale layers as well as a laterally disappearing 5–6 m thick shale layer separating the main Utsira sands body from the overlying Utsira sands wedge (modified after Zweigel et al., 2004).

Table 1. Effective mineral properties for Utsira sands and Nordland shales computed using Hashin-Shtrikman bounds (Hashin and Shtrikman, 1963) from mineral compositions of Utsira sandstone (Chadwick et al., 2004b) and Nordland shale (Bøe and Zweigel, 2001).

Utsira sands	K_s	(GPa)	39.29
	ρ_s	(kg/m^3)	2664
Nordland shales	K_s	(GPa)	22.6
	ρ_s	(kg/m^3)	2390

Table 2. Brine and CO_2 properties in Utsira sands. The values are derived from Batzle and Wang (1992), Lindeberg (2013), and Furre et al. (2015).

Brine	K_w	(GPa)	2.3
	ρ_w	(kg/m^3)	1030
	η_w	(Pa.s)	0.00069
CO_2	K_{CO_2}	(GPa)	0.075
	ρ_{CO_2}	(kg/m^3)	700
	η_{CO_2}	(Pa.s)	0.00006

Table 3. Rock frame properties of Utsira sands derived from Boait et al. (2012), Lindeberg (2013), and Furre et al. (2015).

Rock frame	m		1
	ϕ		0.37
	k_0	(m^2)	2×10^{-12}
	K_D	(GPa)	2.56
	G_D	(GPa)	0.84
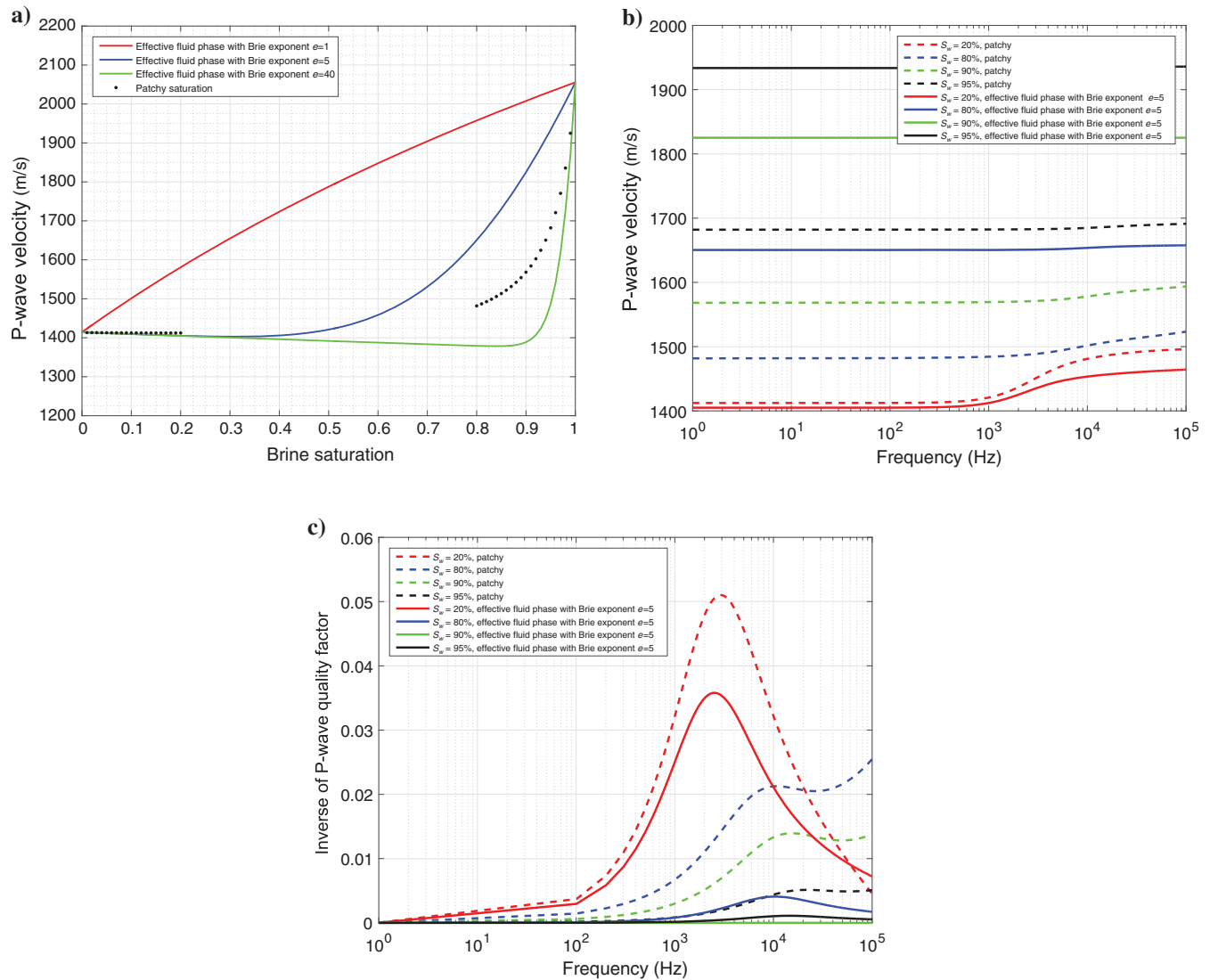
Figure 2. (a) The P-wave velocity versus saturation at 30 Hz for effective fluid phase with different Brie exponents and patchy saturation models. The Voigt upper bound is equivalent to the Brie equation with an exponent equal to one, and the Reuss lower bound is equivalent to the Brie equation with an exponent equal to 40. (b) P-wave velocity and (c) inverse of P-wave quality factor versus frequency for different CO_2 saturations and the two rock physics models (effective fluid phase and patchy saturation). The patchy saturation model is calculated with a patch size equal to 1 cm, whereas the effective fluid phase model is using the Brie equation with n exponent equal to five. It is worth noting that the effective fluid phase requires computation of the effective fluid density (with an arithmetic average) and the effective fluid viscosity (with the Teja and Rice [1981] formulation) in addition to average the fluid bulk modulus (Brie equation).

theory (with three different values of the Brie exponent) and for patchy saturation model. The patchy saturation model is valid for low and high saturations only (see Appendix A). As soon as CO_2 is introduced in the porous medium, a sharp decrease of V_P is observed (fizz-gas effect), whereas the change in velocity is weak when the CO_2 saturation S_{CO_2} is higher than 50%. The velocity decrease is faster when the Brie exponent is high (lower bound) and in case of patchy saturation. On the other hand, the Brie theory with an exponent equal to one (upper bound) provides almost linear velocity behaviour versus saturation changes. This Voigt upper bound is widely used and known as the patchy mixing theory, i.e., that the two fluid phases are assumed not to be mixed at the finest scale. In this case, an effective fluid phase is also estimated, and the effective fluid bulk modulus K_f is used into the Gassmann fluid substitution equation. It is worth noting that using effective fluid phase for patchy mixing combined with Gassmann equation is giving very different results than "advanced" patchy saturation model, which is accounting for physical interactions between fluid phases (Figure 2).

Figure 2b gives V_P from 10 Hz to 100 kHz for different saturation values for patchy saturation with patch size a equal to 1 cm and effective fluid phase with Brie exponent equal to five. According to Figure 2a, the velocity decreases when CO_2 saturation increases. The patchy saturation model also gives lower velocities than effective fluid phase model, except for high CO_2 saturations. The P-wave dispersion is mostly low, except for 20% brine saturation in which dispersion occurs between 1 and 10 kHz. A strong attenuation peak is observed in Figure 2c for $S_w = 20\%$. The P-wave quality factor Q_P reaches 20 at 3 kHz for this high CO_2 saturation. For lower CO_2 saturations, the attenuation peak is located at higher frequencies and the Q_P value is larger (from 50 to very high values). As expected, the attenuation for the patchy saturation model is stronger than the attenuation computed for the effective fluid phase

model. However, at the central frequency of the Sleipner seismic data (approximately 30 Hz), Q_P is greater than 200, regardless of saturation value or distribution. It is worth noting that a different formulation of patchy saturation model using original White equations (White, 1975) provides a P-wave attenuation peak located at seismic frequencies (Carcione et al., 2006; Rubino et al., 2011).

FWI and uncertainty quantification results

A vintage from the 2008 Sleipner data with a maximum offset of 1.8 km was selected to perform 2D FWI. FWI methodology is a well-known seismic imaging technique whose concepts are described in Appendix B. An rms velocity model resulting from velocity analysis was converted into interval velocity in depth and used as a starting model for the inversion. The inversion results (Figure 3) provide clear indications about the geometry and the lateral extent of the thin CO_2 layers and suggests that the inversion has converged to a realistic solution. Because we are considering marine data and because the CO_2 plume is mainly characterized by a fluid change, S-wave impedances within the plume are assumed weak compared with P-wave impedances (Clochard et al., 2010).

Although the obtained velocity image clearly shows the thin layers of gas forming the CO_2 plume at Sleipner (Figure 3), it does not contain any information about the uncertainty in the image. Potentially, other velocity models with a slightly different plume shape, or position, or with different velocity within the imaged layers may explain the observed data and prior information equally well. To quantify such uncertainties, the posterior covariance analysis method described in Appendix B was applied to the FWI results. Because of the high computational cost of calculating the most important eigenvectors (and eigenvalues) of the misfit Hessian for large models, the uncertainty assessment was focused on the area around the plume (see Figure 4).
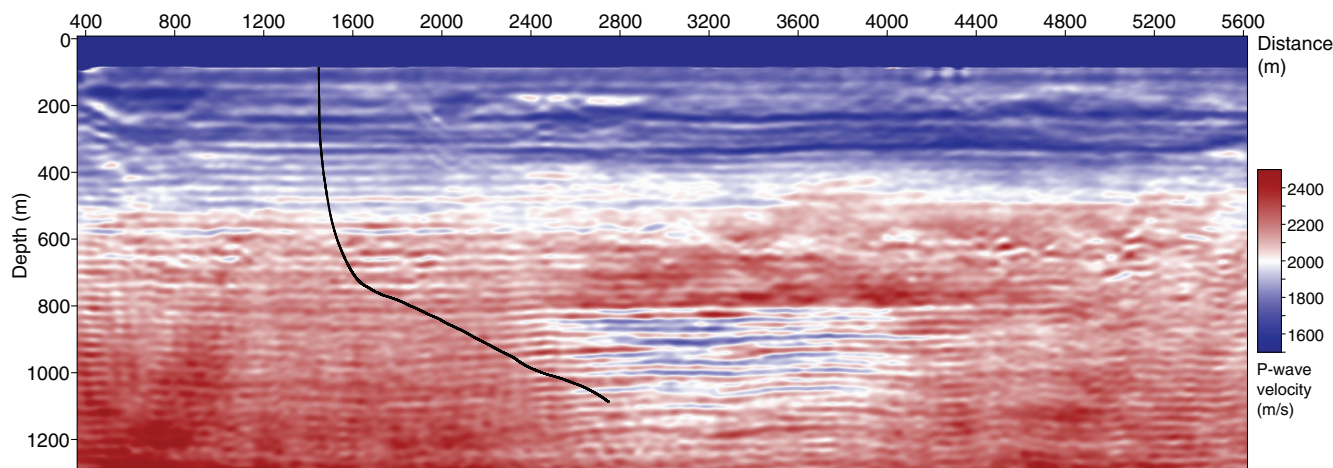

Figure 3. The P-wave velocity model derived from FWI. The black line corresponds to the projection of the injection well into the seismic section. It is worth noting that the 2D section is located 533 m east of the injection point.
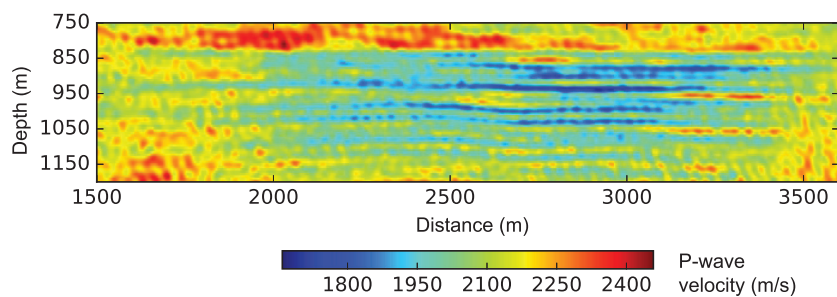
Figure 4. Selected zone from the model recovered by FWI (see Figure 3).
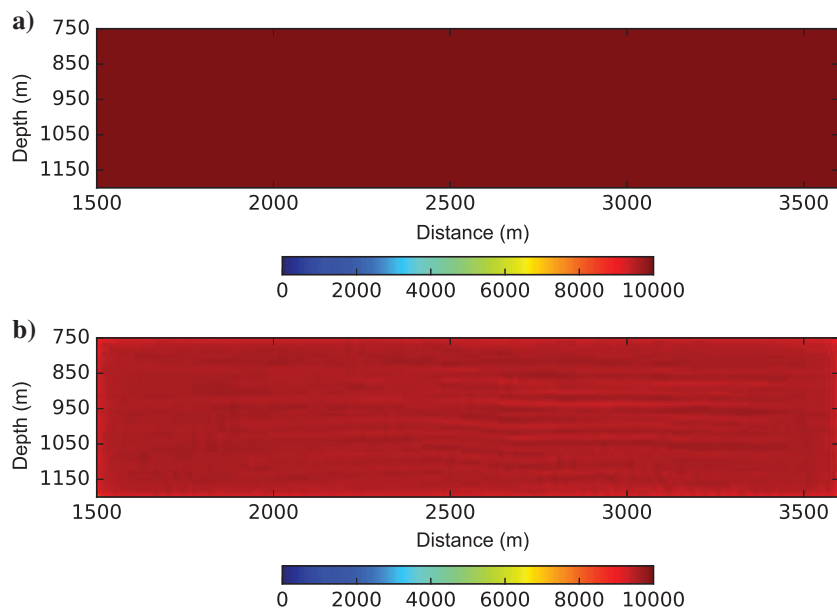
Figure 5. Diagonal of covariance (i.e., variance, $[m^2/s^2]$) mapped to the target (plume) area. (a) Prior variance and (b) posterior variance.
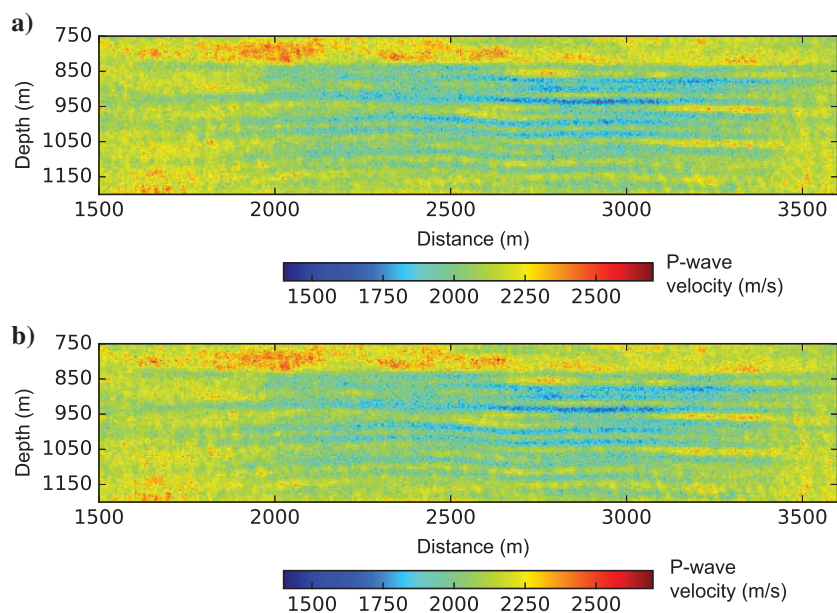
Figure 6. Random samples drawn from the posterior probability distribution.

This region populates a grid of more than 100,000 grid nodes. In addition, more than 10,000 seismic traces were considered. In total, this means that the Hessian contains approximately 10^{10} matrix elements. The Hessian was formed assuming that the measurement quality is the same for all receivers, and the same weight was therefore applied to all misfit components. For the decomposition of the prior-preconditioned Hessian, randomized singular-value decomposition (SVD) was used to be able to do all calculations on a desktop PC within a reasonable time (few hours). The 5000 most important singular vectors and values were calculated. The spectrum of the prior-preconditioned Hessian showed that only a limited number of eigenvalues are significant for the uncertainty analysis (the matrix has an accurate low-rank approximation) and we used the first 4000 for the further studies.

The prior model covariance used in this study was represented by a diagonal matrix with the value 10^4 along the diagonal (see Figure 5a). Using this input, together with the eigenvalues and vectors of the Hessian, the posterior covariance could be efficiently calculated. The posterior covariance was reduced by approximately 10% on average compared with the prior (see Figure 5b). The limited reduction of the covariance, when using the seismic data, may be due to the limited offset (1.8 km) of the available seismic traces and the depth of the imaged plume region. This limits the illumination at depth and consequently the effect that the data have on the posterior covariance.

Using the posterior probability distribution (described by the covariance), several equivalent models were sampled. As shown in Figure 6, these models possess the same main features as the final model from FWI (see Figure 4). Similar results with only slightly larger variance would, however, have been obtained by sampling from the prior. The effect of smoothing regularization was not taken into account in the prior covariance, leading to equivalent models with a noisy appearance. In total, 100 equivalent models were drawn from the posterior distribution. These models were compared with the final model obtained from FWI by plotting depth profiles at the lateral positions $x = 2550$ m (center of target re-
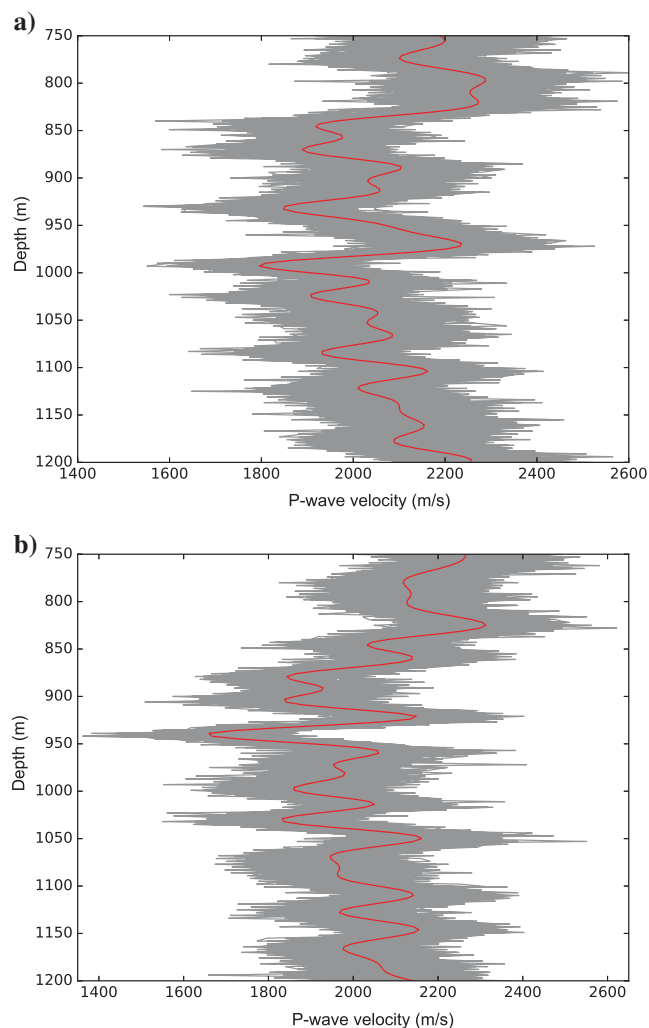
gion) and $x = 2916$ m (where the plume appears to be more saturated) (see Figure 7). These figure parts clearly show that the uncertainty is rather large. Because the smoothing is not part of the prior, the equivalent model velocity profiles are not continuous like the final model.

Rock physics inversion for CO_2 saturation quantification

The rock physics inversion process uses the rock physics models as the forward problem and solves the inverse system using the neighborhood algorithm (NA) (Sambridge, 1999a). More details are given in Appendix C, and examples of the implementation of the rock physics inversion method are given by Dupuy et al. (2016a, 2016b).

Sensitivity tests

Sensitivity tests are carried out to define the accuracy of CO_2 saturation estimates depending on seismic input

data and other a priori properties. Figure 8 gives the results of CO_2 saturation inversion in the most favorable case, i.e., when the other poroelastic properties for solid and fluid phases are assumed to be known (see Tables 1–3). The results are only given for an effective fluid phase model with a Brie exponent equal to five, but the results for the patchy saturation model are similar. When only the P-wave velocity input is available, in case of high CO_2 saturations (low brine saturations), V_P has very low sensitivity with respect to saturation changes (see Figure 2a). The estimation of the correct saturation is therefore highly challenging. We observe in Figure 8a
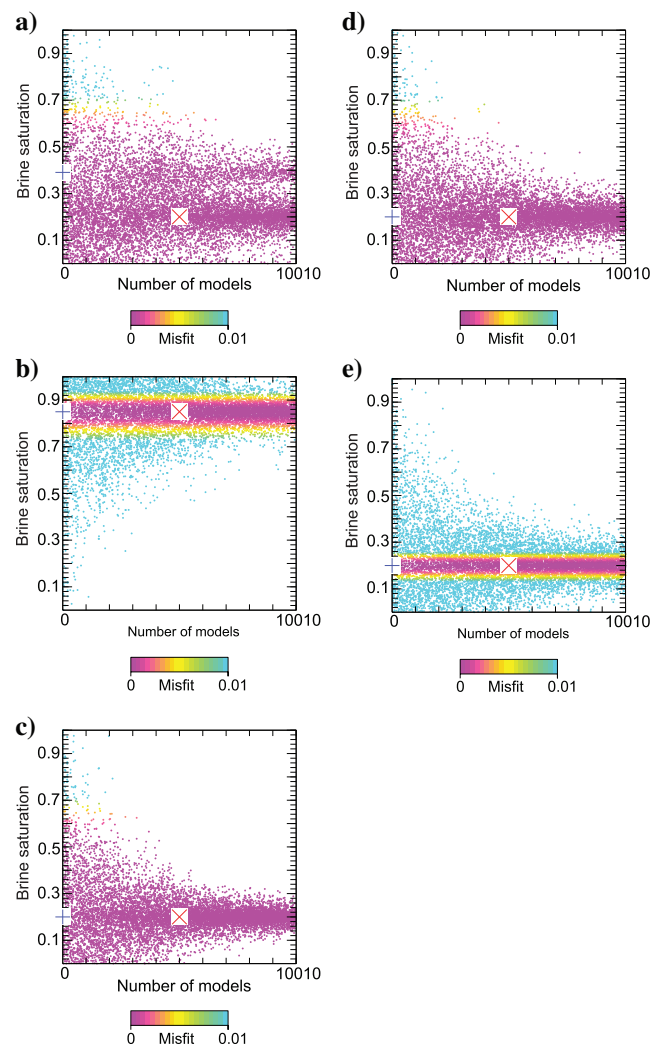
Figure 8. (a) Estimation of brine saturation S_w in the case of an effective fluid phase model using (a and b) V_P input data, (c) V_P and V_S input data, (d) V_P and ρ input data, and (e) V_P and Q_P input data. Panels (a, c, d, and e) give the results for brine saturation equal to 20%, whereas panel (b) is for brine saturation equal to 85%. The panels give the estimated models versus the number of models (10 models sampled at each iteration and 1000 iterations). Each dot represents an inversion model, and the color is related to the absolute misfit value (between 0% and 1%) describing the fit between the observed data and modeled data. The red cross is the true model, whereas the blue cross is the model with the lowest misfit value.
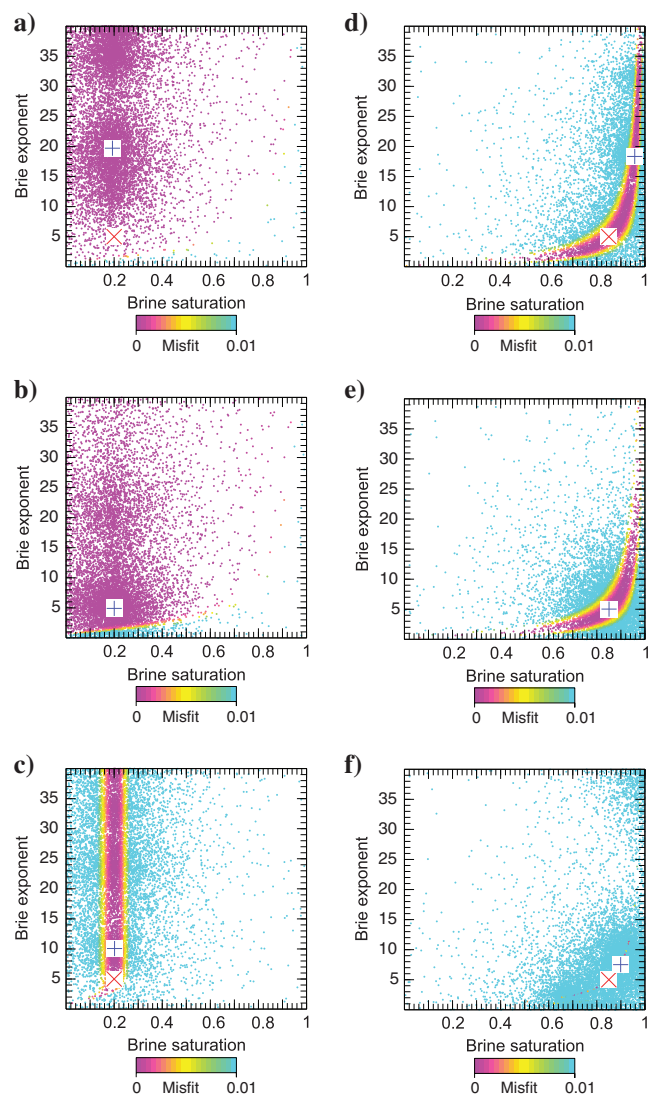

Figure 7. Extracted depth velocity profiles from the posterior distribution at (a) $x = 2550$ m and (b) $x = 2916$ m. The red lines show the 1D velocity profile extracted from the FWI result.

that the low misfit area is wide, between 10% and 40% of brine saturation, and convergence toward the exact model is not easy. However, when considering low CO_2 saturation (Figure 8b), the estimation of saturation is accurate, and the misfit area is narrower. Statistically speaking, we can select a set of models having a misfit lower than 10% and calculate the associated mean and standard deviation values. We conclude that the estimation of CO_2 saturation is well-constrained with a low standard deviation. For high CO_2 saturations, getting an accurate estimate of saturation requires more input data in addition to V_P, for example, shear-wave velocity V_S (Figure 8c), density ρ (Figure 8d), or P-wave quality

factor Q_P (Figure 8e). The standard deviation is lower when using Q_P than when using V_S or ρ.

The previous sensitivity tests are assuming that the rock physics model describing the effective fluid phase is known. The properties of the effective fluid phase are mainly controlled by the effective fluid bulk modulus that can be computed with the Brie equation. Varying the exponent e between 1 and 40 allows spanning the full range of possible effective fluid phase models (see Figure 2a). Figure 9 gives the results for joint estimation of CO_2 saturation and the Brie exponent for low- and high-brine-saturation cases. When only V_P data are available (Figure 9a and 9d), it is difficult to constrain the rock physics model (Brie exponent e) and the saturation simultaneously. In the case of high CO_2 saturation, the estimation of the saturation is surprisingly correct (even if the associated standard deviation is rather large) but the Brie exponent cannot be discriminated between five and 40. When the CO_2 saturation is equal to 15%, the misfit function shape shows the trade-off between S_{CO_2} and exponent e, making it difficult to get the right results for saturation and the Brie exponent. However, when additional input data are taken into account, especially the S-wave velocity V_S (Figure 9b and 9e), the misfit function keeps the same shape but the inversion converges toward the true models. When the P-wave quality factor is added instead of V_S (Figure 9c and 9f), the inversion of S_w and e is better and the standard deviation is lower.

In addition to the rock physics model, another source of uncertainty is related to the knowledge of the in situ pressure and temperature conditions at the Utsira Formation, which might strongly affect some of the CO_2 properties (Ghaderi and Landrø, 2009). We consider the case in which we invert for the CO_2 bulk modulus, viscosity, and density in addition to the saturation. Figure 10 shows the results for (V_P), (V_P, V_S), (V_P, ρ), and (V_P, Q_P) combinations of input data. For the different combinations, complex patterns are observed for the variations of the CO_2 bulk modulus and viscosity. Multiple local minima can be observed when only V_P is considered as an input (Figure 10a). Depending on the selected output pair, wide or elongated misfit function shapes are obtained when other input data are added to V_P (Figure 10b–10d). The estimation of the CO_2 saturation is fairly good for all the cases with a reasonably low standard deviation, and the error in the estimated CO_2 density decreased when two input data were used (from 21% of error using V_P data to 4% of error using V_P and Q_P data and even better when using ρ and V_S with, respectively, 0.64% and 0.02% of error).

Table 4 gives a summary of the three sensitivity tests, taking into account the estimation with the lowest misfit (best model), but also the mean statistical models and associated standard deviations. Analysis of the results suggests that it is possible to provide reliable estimates of the CO_2 saturation even when using only V_P as input. The only exception is the case of high CO_2 saturations because of the low sensitivity of the P-wave velocity to a saturation change in this range (see

Figure 9. (a) Estimation of brine saturation S_w and Brie exponent e in the case of an effective fluid phase model using (a and d) V_P input data, (b and e) V_P and V_S input data, (c and f) V_P and Q_P input data, for panels (a, b, and c) $S_w = 20\%$ and (d, e, and f) $S_w = 85\%$. Each dot represents an inversion model, and the color is related to the absolute misfit value (between 0% and 1%) describing the fit between the observed data and modeled data. The red cross is the true model, whereas the blue cross is the model with the lowest misfit value.

Figure 2). If uncertainties are present on rock physics models (Brie exponent) or on CO_2 properties, additional input data are required to estimate these supplementary parameters even if the saturation estimation stays reliable. Moreover, we observe that the use of V_S data in addition to V_P seems to be more efficient than using density data. On the other hand, using Q_P is crucial to reduce the uncertainty of estimates (lower standard deviation).

Estimation of baseline Utsira sands properties

To accurately estimate CO_2 saturation from seismic data, grains and rock frame properties of Utsira sands need to be defined. We assumed that the CO_2 injection is not modifying these in situ properties. Consequently, we used log data acquired prior to CO_2 injection at Sleipner (well 15/9-A16) to describe the baseline poroelastic properties. The min-

Table 4. Summary of sensitivity tests presented in Figures 8 (second line), 9 (third line), and 10 (fourth line). Symbol ++ means that models with the best misfit and the mean of low misfit models give a correct estimation of the parameter and the associated standard deviation is low. Symbol + means that models with best misfit and mean of low misfit models give correct estimation of parameter but the associated standard deviation is rather large (wide misfit function). Symbol − means that models with best misfit give correct estimation but mean of low misfit models is incorrect and associated standard deviation is large. Symbol −− means that the estimation of the parameter is not correct, and that the inversion is not constrained.

		Input data	V_P	V_P, V_S	V_P, ρ	V_P, Q_P
Rock physics model known	$S_{CO_2} = 80\%$	S_{CO_2}	--	+	+	++
CO_2 properties known	$S_{CO_2} = 15\%$	S_{CO_2}	++			
Rock physics model unknown	$S_{CO_2} = 80\%$	S_{CO_2}	+	+		++
		e	--	-		--
CO_2 properties known	$S_{CO_2} = 15\%$	S_{CO_2}	+	+		+
		e	--	+		+
Rock physics model known		S_{CO_2}	++	++	++	++
	$S_{CO_2} = 15\%$	K_f	--	-	--	-
CO_2 properties unknown		ρ_f	--	-	-	-
		η	-	--	--	--
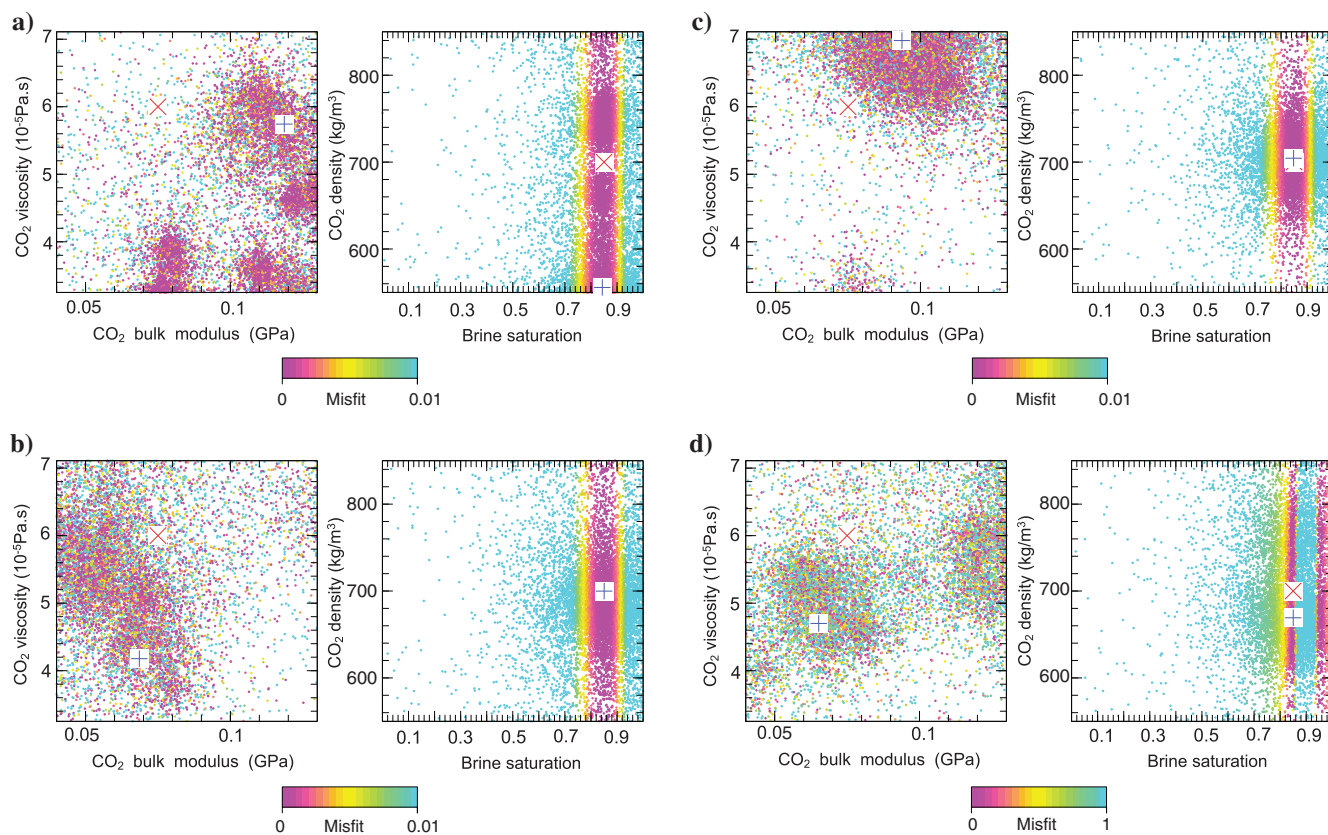
Figure 10. (a) Estimation of CO_2 properties (K_f, ρ_f, and η) and brine saturation S_w in case of an effective fluid phase model using (a) V_P input data, (b) V_P and V_S input data, (c) V_P and ρ input data, and (d) V_P and Q_P input data. The panels give 2D sections of the 4D model space. Each dot represents an inversion model, and the color is related to the absolute misfit value (between 0% and 1%) describing the fit between the observed data and modeled data. For visualization purposes, the results for V_P and Q_P input data (panel d) are plotted between 0% and 100% misfit. The red cross is the true model, whereas the blue cross is the model with the lowest misfit value.

eral grains properties are defined in Table 1 for the Nordland shales and for the Utsira sands, and they are assumed to be constant for the entire section. Before CO_2 injection, the rocks are saturated with brine, whose properties are constant and given in Table 2. Sensitivity tests from Dupuy et al. (2016b) showed that seismic properties are not sensitive to the cementation factor and hydraulic permeability for most common rocks. The cementation factor is taken equal to one for both formations, whereas permeability is derived from log and laboratory data, and it is taken as equal to 1.5×10^{-17} m^2 (0.0172 mdarcy) for the Nordland shales and to 2×10^{-12} m^2 (2.03 darcy) for the Utsira sands. Sensitivity tests suggest that it is better to use a priori values from the porosity log to constrain the inversion of rock frame properties only for dry bulk and shear moduli (Figure 11).

The input data to the inversion are the sonic V_P log, the empirical V_S log derived by the relation of Vernik et al. (2002), and the density log (Figure 11). Figure 11 gives the estimations of dry bulk modulus K_D and shear modulus G_D. We clearly observe the thin interbed shale layers in the Utsira sands. The rock frame properties are otherwise quite homogeneous through the Utsira sands section. The values of the moduli slightly increase with depth, which is the sign of increasing consolidation with increasing burial depth. The quantification of standard

deviation associated with mean models shows that K_D and G_D are estimated with approximately ± 1 GPa uncertainty. This characterization of rock frame properties prior to injection is used as a priori knowledge for CO_2 saturation estimation based on velocity input from seismic vintages acquired after the CO_2 injection started.

Estimation of CO_2 saturation

We extract a 1D vertical profile from the P-wave velocity model obtained by FWI located at the crossing of inline 1881 and crossline 1171, corresponding to the distance 3100 m (see Figure 3), with a focus on the Utsira sands section. Figure 12a gives the comparison between the sonic log data prior to injection and the 1D profile extracted from 2008 FWI study. We clearly see the drops in velocity associated with the interpreted CO_2-bearing layers. A second profile, in which we subtract one standard deviation from the P-wave velocities given by FWI (see Figure 7) is also considered to evaluate the rock physics inversion with the input being more consistent with the velocity estimates provided by Chadwick et al. (2004a). However, it is worth mentioning that the injection well used to acquire the sonic velocity data and the FWI 2D section are not in the same plane. The FWI section is located outside the main CO_2 plume (533 m east of the injection point, where the
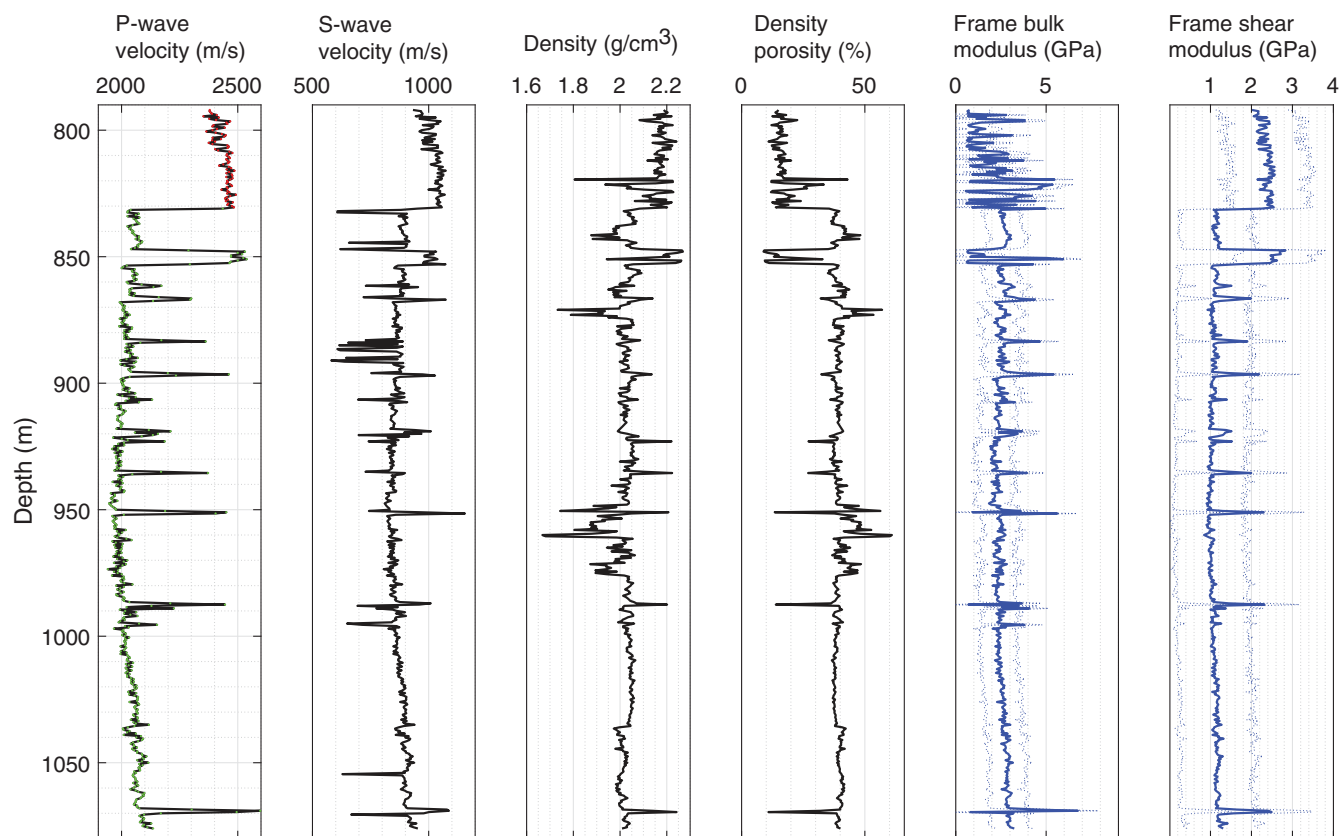
Figure 11. Input log data (black lines) and results of inversion (blue lines), from left to right: P-wave velocity from sonic log data, S-wave velocity derived by Vernik's relation, density log, porosity ϕ from density porosity log, estimated dry bulk modulus K_D, and estimated dry shear modulus G_D. The red dots correspond to the Nordland overburden shale section, whereas the green dots stand for the Utsira sandstone section. The thin blue lines with inverted results show the range of uncertainties in the inversion.

plume shows an north–south elongation), which might explain why the V_P values are higher compared with the expected low values given by Chadwick et al. (2004a) and Furre et al. (2015). In addition, we are comparing two velocities that are recorded at different central frequencies (14 kHz for sonic, 30 Hz for FWI), so the dispersion can play a role as well (see Figure 2b). This dispersion effect is taken into account in the advanced rock physics models used in the rock physics inversion process (see Appendix A).

The a priori properties for the rock physics parameters are defined from baseline data. The grain properties are given in Table 1 and are assumed to be constant for sand and shale sections, whereas the permeability and cementation factors are given in Table 3. The brine and CO_2 properties are given in Table 2 (even if the CO_2 properties are inverted in some tests). The porosity log is the same as the one used for the baseline inversion (Figure 11), and the rock frame moduli are inverted in the baseline test (Figure 11). All the input data are smoothed to match the resolution scale of the velocity profile. Using the P-wave velocity profile extracted from the FWI model and the two partial saturation models (effective fluid phase and patchy saturation models), we estimate the corresponding CO_2 saturations related to the velocity drop (Figure 12b). We observe CO_2 accumulations below shale layers, especially at depths of 850, 870, 900, 950, 980, and 1030 m. The CO_2 saturation ranges from a few percent to a maximum of 30%. When the shifted V_P profile is considered, the CO_2 saturation reaches a maximum of 35% for the upper layer. It is worth noting that the decrease of input velocity equivalent to one standard deviation (approximately 100 m/s) leads to a CO_2 saturation increase of approximately 5%. The patchy saturation model gives lower values than the effective fluid phase model (Figure 12b), but we should remember (see Appendix A) that the patchy saturation model is valid for low and high ranges of saturation only. In this case, the CO_2 saturation is limited between 0% and 20%.

Figure 13 shows additional tests considering different rock physics models and parameterizations of the effective fluid phase model. In addition to the estimation of CO_2 saturation, (1) the Brie exponent is taken as equal to one, five, or 40, (2) the Brie exponent is inverted (range between one and 40), and (3) the CO_2 properties are inverted. The patchy saturation model requires the estimation of the patch size a along with the saturation. All estimations of these additional properties are given in Figure 13b. Figure 13a shows that the patchy mixing case (exponent $e = 1$, upper bound) allows for getting saturations up to 75% in the upper layer and approximately

30%–40% ± 15% in the other sand layers. In the case of uniform saturation ($e = 40$), the CO_2 saturation levels stay low, between 0% and 20% taking into account the uncertainty range. The value of the Brie exponent describes the fluid distribution type for the effective fluid phase (between uniform and patchy mixing), and this is crucial for the CO_2 saturation value (Figure 13a). Figure 13b shows an example in which the Brie exponent is inverted jointly with the CO_2 saturation. We obtain values of saturation going up to 20%–25% with an uncertainty range of 15%, which means that we could reach 40% in the top layer and 30% in the other layers. The value of the Brie exponent is given in Figure 13c and varies between zero and 20 with a mean value of approximately five. This corresponds to an intermediate distribution type, between uniform and patchy mixing. However, the sensitivity tests (Figure 9) have shown that even if the estimation of CO_2 saturation is reliable when using only V_P, the estimation of the Brie exponent is not constrained.

Figure 13b compares patchy saturation models with the patch size fixed or inverted. The results are very similar for both cases, and the saturation is low, approximately 2%–5%. The patch size (when estimated; see Figure 13c) is oscillating around 5 cm with an uncertainty of 2 cm. Figure 13b also shows that the CO_2 saturation estimation is very similar if the CO_2 properties are fixed or inverted, which is in agreement with the sensitivity tests (Figure 10). The CO_2 bulk modulus, density, and viscosity are then estimated jointly, but we have shown that, if only P-wave velocity is available, the inversion of these properties is not well-constrained. Consequently, the values given in Figure 13c should be treated
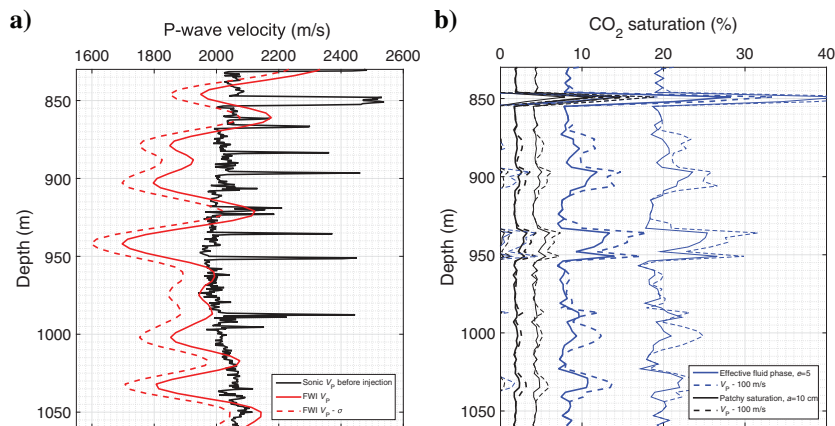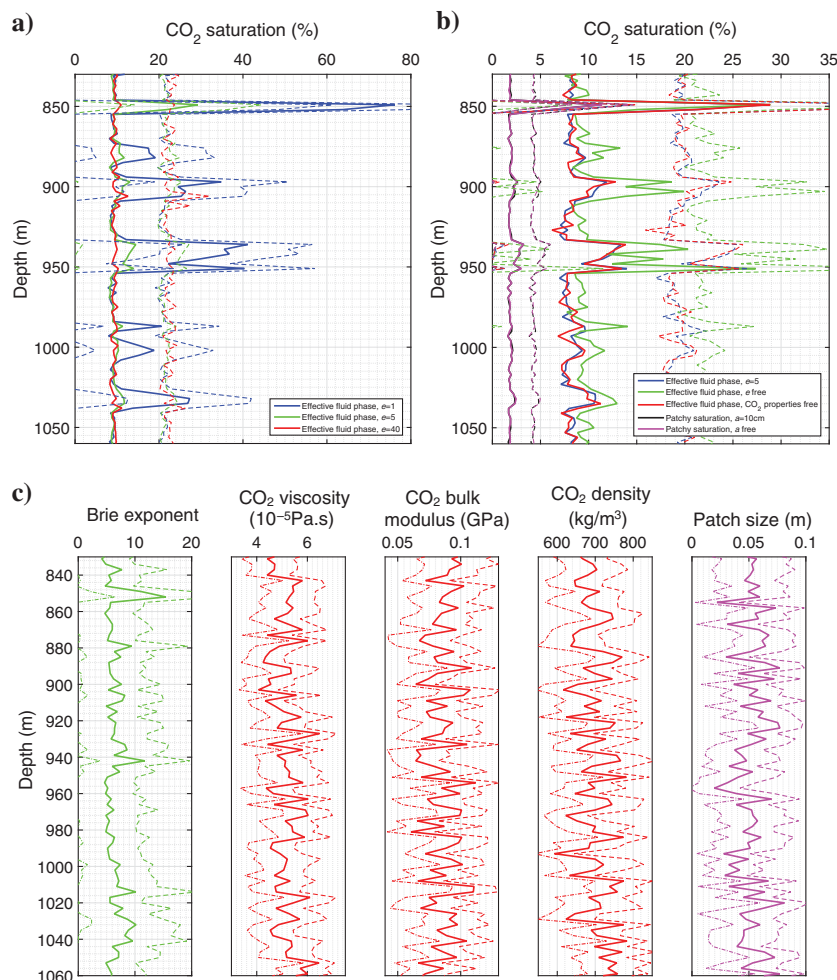

Figure 12. (a) The 1D P-wave velocity profiles from sonic data before CO_2 injection, extracted from FWI result after injection (see Figure 3) and extracted from FWI result minus one standard deviation derived by the uncertainty analysis (see Figure 7). (b) CO_2 saturation estimations using the effective fluid phase model with exponent $e = 5$ (blue lines) and using patchy saturation theory (black lines). The continuous lines stand for the results from V_P values extracted from FWI, whereas the dashed lines stand for the results from V_P values minus one standard deviation derived in the uncertainty analysis (see Figure 7). The thick lines stand for mean results from rock physics inversion, whereas the thin-lines stand for the mean results of rock physics inversion plus/minus one standard deviation derived in the inversion process.

carefully. Even if the CO_2 properties have a big range of uncertainty and cannot be estimated correctly from V_P data only, it is still possible to get reliable estimates of CO_2 saturation and the uncertainty related to the pressure and temperature in the reservoir is not significant.

Discussion

Most of the studies carried out to quantify CO_2 saturations at Sleipner using seismic amplitude interpretation (Chadwick et al., 2010; White et al., 2013; Furre et al., 2015) highlighted the tuning effects challenges related to the thicknesses of the CO_2-bearing layers. In our study, the application of a waveform-based method (FWI) at Sleipner provided clear indications about the geometry and lateral extent of the CO_2 layers being observed as low-velocity thin-layer accumulations. Pre-vious FWI studies showed that it is challenging to recover the correct velocity values of the thin CO_2-filled layers for several reasons. First, FWI performs best when large offsets and low frequencies are available. In our study, streamer data have been used with a maximum available offset of 1800 m. In addition, at high frequencies, the method is indeed more subject to cycle skipping. Furthermore, elastic and eventually viscoelastic effects may need to be considered to provide more reliable estimates of additional properties (S-wave velocity, density, quality factors), which would be very useful to better constrain the rock physics inversion. The strategies to perform multiparameter inversion, however, need to be carefully investigated at Sleipner, due to the complex coupling between the different parameters (Operto et al., 2013). Other interesting perspectives include the use of available geologic information as constraints for the inversion and the application of the method in the time-lapse mode to focus on the changes induced by CO_2 injection (Asnaashari et al., 2015). Obviously, the more information we extract from the available data the better, and with a better constrained velocity model obtained from FWI, we get more reliable input for the rock physics inversion. The value of this type of approach will be significantly increased if the uncertainty in the FWI images can be quantified because this gives us the possibility to determine CO_2 saturation and distribution with a confidence interval.

FWI result gives higher velocity amplitudes (between 1630 and 1750 m/s) compared with those suggested by Chadwick et al. (2010) and Carcione et al. (2006). It can be explained by the fact that it is challenging to recover the true P-wave velocity at the CO_2-bearing layers, as discussed by Romdhane and Querendez (2014), although lateral variations are fairly small. This mismatch is consistent with the observations made in the synthetic study. It can be attributed to some averaging effects while reconstructing the contrasted thin layers given the resolution expected by FWI at 39.5 Hz. The band-limited spectrum of the target zone can also lead FWI to behave more like a least-squares migration. In addition, the 2D section chosen in this test is located 533 m away from the injection point, so we can reasonably assume that the CO_2 saturation is lower than close to the injection point. The uncertainty assessment carried out on FWI results, and based on the work of Eliasson and Romdhane, (2017) showed that the

Figure 13. (a) The CO_2 saturation estimations from FWI result (see Figures 3 and 12a) using effective fluid phase with different Brie exponents. (b) CO_2 saturation estimations from FWI result (see Figures 3 and 12a) using different rock physics models and parameterizations. (c) Brie exponent e, CO_2 viscosity η_{CO_2}, CO_2 bulk modulus K_{CO_2}, CO_2 density ρ_{CO_2}, and patch size a. These additional parameters are inverted jointly with CO_2 saturation (see panel [b]) when using the effective fluid phase and patchy saturation models. The thick lines stand for mean results from rock physics inversion, whereas the thin dash lines stand for the mean results of rock physics inversion plus/minus one standard deviation derived in the inversion process.

P-wave velocity is estimated with an uncertainty range of 100–200 m/s. We show that the CO_2 saturation is only 5% greater when an uncertainty of −100 m/s is taken into account in the input data.

Several existing works have tried to estimate CO_2 saturation at Sleipner using various techniques. Using volumes of injected CO_2 and the link with velocity push-downs, Chadwick et al. (2005) propose that thin layers have high saturations (up to 90%) following the patchy mixing law, whereas lower saturation in form of diffuse CO_2 occur between these layers. On the 2006 vintage, Williams and Chadwick (2012) also estimate very high saturation values. Queißer and Singh (2013) are using FWI results to estimate CO_2 saturation via Gassmann fluid substitution. On the 2006 vintage, they get saturations ranging from 20% (deeper layers) to 90% (870 m deep layer), but P-wave velocities are very low, approximately 1200 m/s. Boait et al. (2012) and Bergmann and Chadwick (2015), using volumetric estimations, derive similar conclusions about the fluid distribution; i.e., the saturation is most likely uniform in high saturation zones and following patchy mixing laws elsewhere. Golding and Huppert (2011) agree with Queißer and Singh (2013) that saturation is probably greater than 30%. Ghosh et al. (2015) quantify the CO_2 saturation with a maximum of 20% for the uniform saturation case and with a maximum of 80% for the patchy mixing case, with an uncertainty of approximately 5%–7%. To mitigate the uncertainty related to a rock physics model, they compare the injected CO_2 mass with the estimated mass corresponding to the two kinds of distributions and they conclude that patchy distribution is more likely. Our saturation estimations are ranging from 5% to 40% or even 75% when considering patchy mixing. The distribution type is not constrained in the inversion, but we think that we are in an intermediate mode, between uniform and patchy mixing. It is worth noting that we are working on the 2008 vintage and that we have selected a 2D section that is more than 500 m away from the injection point.

The sensitivity tests of rock physics inversion showed that the uncertainties related to the saturation type (uniform or patchy) and CO_2 properties (a large range of pressure and temperature in the reservoir) are not preventing correct estimation of CO_2 saturation using only the P-wave velocity input from FWI. However, using additional input data from either multiparameter quantitative seismic imaging (S-wave velocity or P-wave quality factor), or from controlled-source electromagnetic (CSEM) surveys can drastically help the estimation and reduce the uncertainties (Hoversten et al., 2006; Gao et al., 2012; Liang et al., 2016). For example, resistivity is highly sensitive to CO_2 saturation (Park et al., 2013; Eliasson et al., 2014). Even if the resolution of a CSEM resistivity image is lower than FWI results, a combination of seismic and CSEM inputs can be easily implemented via the proposed two-step approach for rock physics inversion (Dupuy et al., 2016a). In addition, the combination of different inputs via joint rock physics inversion will be mandatory for pressure-saturation discrimination. Finally, formulating a Bayesian approach for the rock physics inversion step (using, e.g., the process proposed by Sambridge, 1999b) would allow propagating the uncertainty derived in FWI to the final CO_2 saturation estimates in a proper way.

Conclusion

We have presented extensive work on quantitative seismic characterization of CO_2 saturation and properties at the Sleipner storage site. The quantification was carried out with waveform-based methods, including uncertainty analysis. FWI provided a highly resolved P-wave velocity model with thin low-velocity layers corresponding to the CO_2 accumulations. We showed that we are able to efficiently evaluate the uncertainty in the obtained P-wave velocity model and claim that this information may be very valuable additional input for the rock physics inversion. Large variations of the P-wave velocity with CO_2 saturation were observed depending on the different rock physics models. However, the rock physics inversion sensitivity tests showed that we can get reliable estimates of saturation even if only the P-wave velocity is provided, except if very high CO_2 saturations are considered. The other parameters (such as the CO_2 properties and the Brie exponent representing the saturation distribution type) require additional input data to be correctly estimated, especially the S-wave velocity or P-wave quality factors to get a smaller standard deviation. After the baseline characterization of the rock frame properties based on log data (prior to CO_2 injection), we carried out various tests to estimate CO_2 saturation given the P-wave velocity derived with FWI. We get mean saturations of approximately 10% with a maximum in thin sand layers reaching 30%–35% and up to 75% if pure patchy mixing is considered. However, a joint estimation of the saturation and distribution type (via the Brie exponent) shows that we are more likely located in an intermediate zone between uniform and patchy mixing. In this case, the CO_2 saturations are estimated to be equal to 25% ± 15%. Using the advanced patchy saturation model, the CO_2 saturation is ranging between 2% and 5%. The CO_2 properties are not well-constrained but do not affect the saturation estimates.

Acknowledgments

Appendix A
Rock physics models

Porous media homogenization

For porous media, an homogenization approach for fluid and solid phases allows building an equivalent medium at the wavelength scale (Burridge and Vargas, 1979). Considering grains properties (solid grains bulk modulus K_s and grains density ρ_s) and fluid phase properties (fluid bulk modulus K_f, fluid density ρ_f, and fluid viscosity η), we can describe microscale fluid and solid properties. The arrangement of the solid grains provides a set of mesoscale properties that are also used in the effective medium building: porosity ϕ, hydraulic permeability k_0, cementation factor m, dry bulk modulus K_D, and dry shear modulus G_D. Several effective medium theories can be used to compute the effective mechanical moduli K_D and G_D (Berryman, 1995; Mavko et al., 2009). This set of nine parameters is the input in the Biot-Gassmann rock physics model (Gassmann, 1951; Biot, 1956a, 1956b).

The density of the porous medium is the arithmetic mean of the fluid and solid phases weighted by their own volumes via the porosity, such that

$$\rho = (1 - \phi)\rho_s + \phi\rho_f. \tag{A-1}$$

Auriault et al. (1985) and Johnson et al. (1987) generalize Darcy's law with a dynamic permeability $k(\omega)$ that depends on the angular frequency ω, which is written using the dispersive relation (i is the complex number):

$$k(\omega) = \frac{k_0}{\sqrt{1 - \frac{1}{2} i \frac{\omega}{\omega_c} - i \frac{\omega}{\omega_c}}}. \tag{A-2}$$

The characteristic angular frequency ω_c makes it possible to separate the low-frequency domain in which viscous effects are dominant from the high-frequency domain in which inertial effects prevail. Using Archie's law (Adler et al., 1992), the angular frequency ω_c can be defined as

$$\omega_c = \frac{i\eta}{\rho_f k_0 \phi^{-m}}, \tag{A-3}$$

where the cementation exponent m is related to the formation factor (Adler et al., 1992) and to the pore tortuosities (Brown, 1980). Then, the flow resistance density term $\tilde{\rho}(\omega)$ describes the dynamic loss of energy due to the fluid flow with an explicit frequency dependence. This accounts for the intrinsic scattering of waves in the Biot poroelasticity theory (Biot, 1956a, 1956b) and is expressed as

$$\tilde{\rho}(\omega) = \frac{i\eta}{\omega k(\omega)}. \tag{A-4}$$

The introduction of the undrained bulk modulus K_U, the Biot C modulus, and the fluid storage coefficient M makes it possible to explicitly describe the homogenized porous medium through Biot (1956a, 1956b) and Gassmann (1951) relations. Relationships between moduli K_U, C, and M and the parameters K_D, K_s, K_f, and ϕ are given by

$$K_U = \frac{\phi K_D + (1 - (1 + \phi)K_D/K_s)K_f}{\phi(1 + \Delta)},$$
$$C = \frac{(1 - K_D/K_s)K_f}{\phi(1 + \Delta)},$$
$$M = \frac{K_f}{\phi(1 + \Delta)}, \tag{A-5}$$

where

$$\Delta = \frac{1 - \phi}{\phi} \frac{K_f}{K_s} \left(1 - \frac{K_D}{(1 - \phi)K_s}\right). \tag{A-6}$$

The shear modulus G of the porous medium is assumed to be independent of the fluid characteristics and equal the shear modulus of the drained solid frame G_D.

Partial saturation
Effective fluid phase

To consider partially saturated media, a conventional approach consists of building an effective fluid phase and to apply the Biot-Gassmann theory for a saturated medium. Domenico (1976) and Berryman et al. (2000) propose to compute equivalent parameters by weighted averaging using the volume fraction of the fluid phase, i.e., brine saturation S_w and CO_2 saturation S_{CO_2}. For densities, we use a weighted arithmetic average (Voigt, 1889):

$$\rho_f = S_w \rho_w + S_{CO_2} \rho_{CO_2}. \tag{A-7}$$

For the bulk fluid moduli, the weighted arithmetic (Voigt, 1889) and harmonic (Reuss, 1929) averages provide the lower and upper bounds; i.e., the fluid phases are mixed at the finest scale (uniform mixing), or the more mobile fluid is shaped as patches (patchy mixing), respectively. For a liquid/gas mixture, we can vary the exponent of Brie et al. (1995) equation to span the full range of models for effective fluid bulk modulus, between the lower and upper bounds. Brie et al. (1995) formulate the effective K_f as

$$K_f = (K_w - K_{CO_2})S_w^e + K_{CO_2}, \tag{A-8}$$

where the subscript w denotes the brine phase and CO_2 subscript denotes the carbon dioxide phase. The exponent e can vary from 1 (upper bound) to 40 (lower bound). For viscosity, Teja and Rice (1981) suggest a formula (also used by Carcione et al., 2006) to compute the effective viscosity η as

$$\eta = \eta_{CO_2} \left(\frac{\eta_w}{\eta_{CO_2}} \right)^{S_w}. \qquad (A\text{-}9)$$

Patchy saturation

In partially saturated media (water and air, gas and oil, water and CO_2, ...), the mechanical (K_f), inertial (ρ_f and $\tilde{\rho}(\omega)$), and viscous (η) fluid terms can vary from several orders of magnitude (Batzle and Wang, 1992; Mavko et al., 2009). Indeed, if two immiscible fluids are saturating the solid matrix, the repartition of the two fluid phases is built with a patchy configuration. When a pressure wave goes through the medium, the fluid flow due to the equilibration of pressure gradients is different in each fluid phase. White (1975) and Dutta and Odé (1979) offer to model saturation areas by spherical inclusions. From the two fluids equations of state, Pride et al. (2004) describe the motions of the two fluids and their interactions with the porous solid phase. The a_{ij} constants ($i, j \in (1, 3)$) are the components of the generalized rigidity matrix, and they are expressed with the following relations (Pride et al., 2004):

$$a_{11} = \frac{1}{K_{D_0}},$$
$$a_{22} = (-\beta + S_w/B_w) \frac{\alpha}{K_{D_0}},$$
$$a_{33} = (-\beta + S_{CO_2}/B_{CO_2}) \frac{\alpha}{K_{D_0}},$$
$$a_{12} = -\frac{S_w \alpha}{K_{D_0}},$$
$$a_{13} = -\frac{S_{CO_2} \alpha}{K_{D_0}},$$
$$a_{23} = \frac{\beta \alpha}{K_{D_0}}, \qquad (A\text{-}10)$$

where B_w and B_{CO_2} are the Skempton moduli for porous media saturated by each fluid phase, computed by Gassmann (1951) relations. Pride et al. (2004) determine the β parameter with a high-frequency approximation. This allows considering undrained patches and allows to apply elasticity laws to the composite material. The parameter β is then equal to

$$\beta = \left(\frac{S_w S_{CO_2}}{B_w B_{CO_2}} \right) \frac{S_w B_w + S_{CO_2} B_{CO_2} - 1/\alpha + K_{D_0}/K_H}{1 - (1/\alpha - K_{D_0}/K_H)(S_w/B_w + S_{CO_2}/B_{CO_2})}, \qquad (A\text{-}11)$$

where K_{D_0} is the bulk drained modulus computed by harmonic average for the effective medium and K_H is the elastic modulus of the composite as

$$K_H = 1/\left[\frac{S_w}{K_{D_0}/(1 - \alpha B_w) + 4G/3} \right.$$
$$\left. + \frac{S_{CO_2}}{K_{D_0}/(1 - \alpha B_{CO_2}) + 4G/3} \right]. \qquad (A\text{-}12)$$

The internal transport coefficient $\gamma(\omega)$, depending on γ_p and ω_p, is given by Pride et al. (2004). This coefficient describes the behavior law of fluid transfers, which depends on capillarity effects and on interphase mesoscopic flows. The expression is

$$\gamma(\omega) = \gamma_p \sqrt{1 - \frac{i\omega}{\omega_p}}, \qquad (A\text{-}13)$$

with

$$\gamma_p = \frac{S_w k_0}{\eta_w L_1^2},$$
$$\omega_p = \frac{K_{D_0} B_w}{\eta_w \alpha} \frac{k_0 S_w^2 (V/S)^2}{L_1^4} \left(1 + \sqrt{\frac{\eta_{CO_2} B_{CO_2}}{\eta_w B_w}} \right)^2. \qquad (A\text{-}14)$$

Two geometric terms appear in these previous equations: L_1 and V/S. The term S is the contact surface between fluids in an elemental volume V and L_1 is the distance in the phase 1 so that the pressure gradient is canceled. Phase 1 is the phase with the lowest mobility. The mobility is proportional to the ratio k_0/η. If we consider that each fluid patch has a sphere shape with a radius a, we can deduce analytic solutions for V/S and L_1. Pride et al. (2004) develop three cases depending of the fluid proportions:

- $S_{CO_2} \ll S_w$: As an example, a medium saturated with brine at 90%, the most mobile is the CO_2 phase ($S_{CO_2} = 0, 1$) and so, we can check the criterion η_{CO_2}/η_w low. The CO_2 phase is described by spheres with a radius equal to a, inserted in spheres with a radius of R. We deduce $V/S = R^3/3a^2 = aS_{CO_2}/3$ and $L_1^2 = 9S_{CO_2}^{-2/3} a^2 (1 - 7S_{CO_2}^{1/3}/6)/14$. Because the CO_2 phase is in a low quantity, it is assumed to be immobile with respect to the solid matrix and the following approximations are considered: $\rho_f = \rho_w$ (but keeping $\rho = (1 - \phi)\rho_s + \phi (S_w \rho_w + S_{CO_2} \rho_{CO_2})$) and $\tilde{\rho}(\omega) = i\eta_w/(\omega k(\omega))$.
- $S_w \ll S_{CO_2}$: On the contrary, the more mobile phase is predominant, the geometric parameters are $V/S = aS_w/3$ and $L_1^2 = a^2/15$, and we assume $\rho_f = \rho_{CO_2}$ and $\tilde{\rho}(\omega) = i\eta_{CO_2}/(\omega k(\omega))$.
- If S_w and S_{CO_2} have the same order in magnitude, we cannot deduce analytic solutions.

To justify these semiempirical assumptions, Pride et al. (2004) show an excellent agreement between their re-

sults and that of Johnson (2001). To follow these assumptions, we restrict the CO_2 saturation between 0% and 20% in the case of patchy saturation.

Finally, we compute equivalent mechanical moduli ($K_U(\omega)$, $G(\omega)$, $C(\omega)$, and $M(\omega)$) that are frequency dependent and that describe the complex medium for each scale/frequency. Pride et al. (2004) formulate the bulk drained modulus $K_D(\omega)$, the bulk undrained modulus $K_U(\omega)$, and the Skempton modulus $B(\omega)$ for the effective medium as

$$
\frac{1}{K_D(\omega)} = a_{11} - \frac{a_{13}^2}{a_{33} - \gamma(\omega)},
$$
$$
B(\omega) = \frac{-a_{12}(a_{33} - \gamma(\omega)) + a_{13}(a_{23} + \gamma(\omega))}{(a_{22} - \gamma(\omega))(a_{33} - \gamma(\omega)) - (a_{23} + \gamma(\omega))^2},
$$
$$
\frac{1}{K_U(\omega)} = \frac{1}{K_D(\omega)} + B(\omega)\left(a_{12} - \frac{a_{13}(a_{23} + \gamma(\omega))}{a_{33} - \gamma(\omega)}\right). \quad \text{(A-15)}
$$

The moduli $K_U(\omega)$, $C(\omega)$, and $M(\omega)$ are then deduced from equation A-15 as

$$
K_U(\omega) = \left[\frac{1}{K_D(\omega)} + B(\omega)\left(a_{12} - \frac{a_{13}(a_{23} + \gamma(\omega))}{a_{33} - \gamma(\omega)}\right)\right]^{-1},
$$
$$
C(\omega) = B(\omega)K_U(\omega),
$$
$$
M(\omega) = B(\omega)\frac{K_U(\omega)}{\alpha}, \quad \text{(A-16)}
$$

where the Biot-Willis constant is $\alpha = 1 - K_{D_0}/K_s$. The function $G(\omega)$ is assumed to be frequency independent and is equal to the drained shear modulus: $G(\omega) = G_D$. This assumption is valid in the seismic frequency band in which squirt flow mechanisms are negligible, but the frequency dependence should be considered at ultrasonic frequencies (Chapman, 2003).

Viscoelastic properties

The Biot poroelastodynamic theory (Biot, 1956a, 1956b) gives relations for the slowness of the P- and S-wave (Pride, 2005). The S-wave slowness is derived as

$$
s_S^2(\omega) = \frac{\rho - \rho_f^2/\tilde{\rho}(\omega)}{G}, \quad \text{(A-17)}
$$

whereas the P-wave slowness is given by

$$
s_P^2(\omega) = \frac{\gamma(\omega)}{2} - \frac{1}{2}\sqrt{\gamma^2(\omega) - \frac{4(\rho\tilde{\rho}(\omega) - \rho_f^2)}{H(\omega)M(\omega) - C^2(\omega)}}, \quad \text{(A-18)}
$$

where γ and H are

$$
\gamma(\omega) = \frac{\rho M(\omega) + \tilde{\rho}(\omega)H(\omega) - 2\rho_f C(\omega)}{H(\omega)M(\omega) - C^2(\omega)},
$$
$$
H(\omega) = K_U(\omega) + \frac{4}{3}G. \quad \text{(A-19)}
$$

Now, we can deduce the effective viscoelastic velocities and quality factors for P- and S-waves as

$$
V_{P,S}(\omega) = \frac{1}{\mathcal{Re}(s_{P,S}(\omega))}.
$$
$$
Q_{P,S}(\omega) = \frac{\mathcal{Re}(s_{P,S}^2(\omega))}{\mathcal{Im}(s_{P,S}^2(\omega))}. \quad \text{(A-20)}
$$

The viscoelastic velocities (V_P and V_S) and quality factors (Q_P and Q_S), as well as the mean density ρ, are the effective properties (or seismic attributes) that describe the behavior of the medium at the macroscale (wavelength), and their combination will provide inputs to the rock physics inverse problem.

Appendix B
FWI and uncertainty assessment

FWI is based on a data fitting process in which a model vector is updated to minimize the misfit between modeled and observed data. The forward problem (modeling of the seismic response given the subsurface properties) is solved in the frequency-space domain, as described by Hustedt et al. (2004). The inverse problem (estimation of selected subsurface properties given a recorded seismic response) is formulated as a least-squares local optimization and solved iteratively using a preconditioned gradient method, as described by Ravaut et al. (2004) and Romdhane and Querendez (2014). The inversion is carried out by proceeding iteratively from low to high frequencies to mitigate cycle skipping and allow shorter wavelengths to be introduced progressively in the parameter images. Thus, this helps to reduce the risk that the optimization gets trapped in a local minimum.

To quantify the uncertainty in the images obtained with FWI, we use a method based on the computation of the inverse of the Hessian, which can be interpreted as the posterior covariance matrix in a local probabilistic sense. Due to computational costs, the Hessian is often approximated (Métivier et al., 2013; Amaya et al., 2016) and so is the posterior covariance. The method used by Zhu et al. (2016) and Eliasson and Romdhane (2017) is valid in the vicinity of the global solution. The approximation of the posterior covariance is obtained using the Gauss-Newton approximation and the low-rank property of the so-called prior-preconditioned Hessian (Bui-Thanh et al., 2013), which is decomposed using randomized SVD (Halko et al., 2011) for computational efficiency. This leads to a posterior covariance calculated as a reduction of the prior covariance by a term based on the information gained from available geophysical data (Bui-Thanh et al., 2013). The posterior covariance matrix can be used to generate "equivalent" models, which explain the observed data equally well (taking noise and other prior information into account) as the final FWI model. More details of the complete formulation can be found in Eliasson and Romdhane (2017).

Appendix C

Rock physics inversion

The inverse problem consists of the extraction of models (poroelastic micro/mesoscale parameters) from input data (viscoelastic seismic attributes), and it is formulated as

$$\mathbf{d} = g(\mathbf{m}), \qquad \text{(C-1)}$$

where $\mathbf{d}$ is the data vector, $\mathbf{m}$ is the model vector, and g is a nonlinear function linking models and data. In our approach, the function g contains the analytical Biot-Gassmann relations (see Appendix A), which compute P- and S-wave velocities and quality factors and the mean density with respect to the poroelastic parameters (described in Appendix A). This function is nonlinear, and the inverse of g cannot be computed. The solution of the inverse system can be obtained by global or semiglobal optimization methods because the computation of the forward model is very fast. The global optimization methods search for the global minimum of the misfit function over the whole model domain, avoiding convergence toward a local minimum. We use an oriented Monte Carlo method called neighborhood algorithm, which is guided toward the best models to reduce computational costs (Sambridge, 1999a). The optimization aims to minimize a scalar function (misfit function) describing the discrepancy between observed data $\mathbf{d}_{\text{obs}}$ and calculated data $g(\mathbf{m})$ (by forward modeling). We use an L_2 norm to compute the misfit $C(\mathbf{m})$ as

$$C(\mathbf{m}) = \frac{1}{2}[(\mathbf{d}_{\text{obs}} - g(\mathbf{m}))^T(\mathbf{d}_{\text{obs}} - g(\mathbf{m}))]. \qquad \text{(C-2)}$$

The principle of the NA consists of dividing the model space into Voronoï cells at each iteration to focus the resampling with respect to the lower misfit function values. For each iteration, new cells are computed with respect to previous sample misfit values. The resampling is then focused on the lower misfit areas. The different tests run by Dupuy et al. (2016b) show that no regularization is needed. The initial range for each parameter defines the model space. The number of iterations varies between 400 and 1000, and a resampling factor of 10 is applied at each iterations, which means that between 4010 and 10,010 models are computed for each inversion case.

References

Adler, P., C. Jacquin, and J.-F. Thovert, 1992, The formation factor of reconstructed porous media: Water Resources Research, **28**, 1571–1576, doi: 10.1029/92WR00059.

Amaya, M., J. Morten, and L. Boman, 2016, A low-rank approximation for large-scale 3D controlled-source electromagnetic Gauss-Newton inversion: Geophysics, **81**, no. 3, E211–E225, doi: 10.1190/geo2015-0079.1.

Arts, R., O. Eiken, A. Chadwick, P. Zweigel, L. van der Meer, and B. Zinszner, 2004, Monitoring of CO_2 injected at Sleipner using time-lapse seismic data: Energy, **29**, 1383–1392, doi: 10.1016/j.energy.2004.03.072.

Asnaashari, A., R. Brossier, S. Garambois, F. Audebert, P. Thore, and J. Virieux, 2015, Time-lapse seismic imaging using regularized full waveform inversion with prior model: Which strategy?: Geophysical Prospecting, **63**, 78–98, doi: 10.1111/1365-2478.12176.

Auriault, J.-L., L. Borne, and R. Chambon, 1985, Dynamics of porous saturated media, checking of the generalized law of Darcy: Journal of Acoustical Society of America, **77**, 1641–1650, doi: 10.1121/1.391962.

Batzle, M., and Z. Wang, 1992, Seismic properties of pore fluids: Geophysics, **57**, 1396–1408, doi: 10.1190/1.1443207.

Bergmann, P., and A. Chadwick, 2015, Volumetric bounds on subsurface fluid substitution using 4D seismic time shifts with an application at Sleipner, North Sea: Geophysics, **80**, no. 5, B153–B165, doi: 10.1190/geo2014-0591.1.

Berryman, J., 1995, Mixture theories for rock properties, *in* T. J. Ahrens, ed., Rock physics and phase relations: A handbook of physical constants: AGU Ref. Shelf: AGU 2.

Berryman, J., P. Berge, and B. Bonner, 2000, Transformation of seismic velocity data to extract porosity and saturation values for rocks: Journal of Acoustical Society of America, **107**, 3018–3027, doi: 10.1121/1.429331.

Biot, M., 1956a, Theory of propagation of elastic waves in a fluid-saturated porous solid. II. Higher frequency range: Journal of the Acoustical Society of America, **28**, 179–191, doi: 10.1121/1.1908241.

Biot, M., 1956b, Theory of propagation of elastic waves in a fluid-saturated porous solid. I. Low-frequency range: Journal of Acoustical Society of America, **28**, 168–178, doi: 10.1121/1.1908239.

Boait, F. C., N. J. White, M. J. Bickle, R. A. Chadwick, J. A. Neufeld, and H. E. Huppert, 2012, Spatial and temporal evolution of injected CO_2 at the Sleipner Field, North Sea: Journal of Geophysical Research: Solid Earth, **117**, B03309, doi: 10.1029/2011JB008603.

Bøe, R., and P. Zweigel, 2001, Characterisation of the Nordland Shale in the Sleipner area by XRD analysis: A contribution to the Saline Aquifer CO_2 Storage (SACS) project: SINTEF Report, 1–23.

Brie, A., F. Pampuri, A. Marsala, and O. Meazza, 1995, Shear sonic interpretation in gas-bearing sands: Presented at the SPE Annual Technical Conference and Exhibition, 701–710.

Brown, R., 1980, Connection between formation factor for electrical resistivity and fluid- solid coupling factor for Biot's equation in fluid filled porous media: Geophysics, **45**, 1269–1275, doi: 10.1190/1.1441123.

Brown, S., G. Bussod, and P. Hagin, 2007, AVO monitoring of CO_2 sequestration: A benchtop-modeling study: The Leading Edge, **26**, 1576–1583, doi: 10.1190/1.2821945.

Buddensiek, M. L., S. Sturton, and M. Dillen, 2010, AVO analysis of thin layers: Applications to CO_2 storage at Sleipner: 72nd Annual International Conference and Exhibition, EAGE, Extended Abstracts, doi: 10.3997/2214-4609.201401190.

Bui-Thanh, T., O. Ghattas, J. Martin, and G. Stadler, 2013, A computational framework for infinite-dimensional Bayesian inverse problems — Part I: The linearized case, with application to global seismic inversion: SIAM Journal on Scientific Computing, **35**, A2494–A2523, doi: 10.1137/12089586X.

Burridge, R., and C. Vargas, 1979, The fundamental solution in dynamic poroelasticity: Geophysical Journal of the Royal Astronomical Society, **58**, 61–90, doi: 10.1111/j.1365-246X.1979.tb01010.x.

Carcione, J., S. Picotti, D. Gei, and G. Rossi, 2006, Physics and seismic modeling for monitoring CO_2 storage: Pure and Applied Geophysics, **163**, 175–207, doi: 10.1007/s00024-005-0002-1.

Causse, E., M. Riede, A. J. van Wijngaarden, A. Buland, J. F. Dutzer, and R. Fillon, 2007, Amplitude analysis with an optimal model-based linear AVO approximation — Part II: Field data example: Geophysics, **72**, no. 3, C71–C79, doi: 10.1190/1.2712176.

Chadwick, A., G. Williams, N. Delepine, V. Clochard, K. Labat, S. Sturton, M.-L. Budden-siek, M. Dillen, M. Nickel, A.-L. Lima, R. Arts, F. Neele, and G. Rossi, 2010, Quantitative analysis of time-lapse seismic monitoring data at the Sleipner CO_2 storage operation: The Leading Edge, **29**, 170–177, doi: 10.1190/1.3304820.

Chadwick, R., R. Arts, and O. Eiken, 2005, 4D seismic quantification of a growing CO_2 plume at Sleipner, North Sea: Geological Society, Petroleum Geology Conference Series, 1385–1399.

Chadwick, R., R. Arts, O. Eiken, G. Kirby, E. Lindeberg, and P. Zweigel, 2004a, 4D seismic imaging of an injected CO_2 plume at the Sleipner field, central North Sea: Geological Society, London, Memoirs, **29**, 311–320, doi: 10.1144/GSL.MEM.2004.029.01.29.

Chadwick, R., P. Zweigel, U. Gregersen, G. Kirby, S. Holloway, and P. Johannessen, 2004b, Geological reservoir characterization of a CO_2 storage site: The Utsira Sand, Sleipner, northern North Sea: Energy, **29**, 1371–1381, doi: 10.1016/j.energy.2004.03.071.

Chapman, M., 2003, Frequency dependent anisotropy due to meso-scale fractures in the presence of equant porosity: Geophysical Prospecting, **51**, 369–379, doi: 10.1046/j.1365-2478.2003.00384.x.

Clochard, V., N. Delépine, K. Labat, and P. Ricarte, 2010, CO_2 plume imaging using 3D pre-stack stratigraphic inversion: A case study on the Sleipner field: First Break, **28**, 91–96.

Domenico, S. N., 1976, Effect of brine-gas mixture on velocity in an uncosolidated sand reservoir: Geophysics, **41**, 882–894, doi: 10.1190/1.1440670.

Duffet, C., and D. Sinoquet, 2006, Quantifying uncertainties on the solution model of seismic tomography: Inverse Problems, **22**, 525–538, doi: 10.1088/0266-5611/22/2/009.

Dupuy, B., S. Garambois, A. Asnaashari, H. M. Balhareth, M. Landrø, A. Stovas, and J. Virieux, 2016a, Estimation of rock physics properties from seismic attributes —

Part II: Applications: Geophysics, **81**, no. 4, M55–M69, doi: 10.1190/geo2015-0492.1.

Dupuy, B., S. Garambois, and J. Virieux, 2016b, Estimation of rock physics properties from seismic attributes — Part I: Strategy and sensitivity analysis: Geophysics, **81**, no. 3, M35–M53, doi: 10.1190/geo2015-0239.1.

Dutta, A. J., and H. Odé, 1979, Attenuation and dispersion of compressional waves in fluid-filled porous rocks with partial gas saturation (White model) —Part I: Biot theory: Geophysics, **44**, 1777–1788, doi: 10.1190/1.1440938.

Eliasson, P., and A. Romdhane, 2017, Uncertainty evaluation in waveform-based imaging methods: A case study at Sleipner: 79th Annual International Conference and Exhibition, EAGE, Extended Abstracts, doi: 10.3997/2214-4609.201701317.

Eliasson, P., A. Romdhane, M. Jordan, and E. Querendez, 2014, A synthetic Sleipner study of CO_2 quantification using controlled source electro-magnetics and full waveform inversion: Energy Procedia, **63**, 4249–4263, doi: 10.1016/j.egypro.2014.11.460.

Fernández-Martínez, J. L., 2015, Model reduction and uncertainty analysis in inverse problems: The Leading Edge, **34**, 1006–1016, doi: 10.1190/tle34091006.1.

Fernández-Martínez, J. L., Z. Fernández-Muñiz, J. Pallero, and L. M. Pedruelo-González, 2013, From Bayes to Tarantola: New insights to understand uncertainty in inverse problems: Journal of Applied Geophysics, **98**, 62–72, doi: 10.1016/j.jappgeo.2013.07.005.

Fichtner, A., and J. Trampert, 2011, Resolution analysis in full waveform inversion: Geophysical Journal International, **187**, 1604–1624, doi: 10.1111/j.1365-246X.2011.05218.x.

Furre, A.-K., and O. Eiken, 2014, Dual sensor streamer technology used in Sleipner CO_2 injection monitoring: Geophysical Prospecting, **62**, 1075–1088, doi: 10.1111/1365-2478.12120.

Furre, A.-K., A. Kir, and O. Eiken, 2015, CO_2-induced seismic time shifts at Sleipner: Interpretation, **3**, SS23–SS35, doi: 10.1190/INT-2014-0225.1.

Gao, G., A. Abubakar, and T. M. Habashy, 2012, Joint petrophysical inversion of electromagnetic and full-waveform seismic data: Geophysics, **77**, no. 3, WA3–WA18, doi: 10.1190/geo2011-0157.1.

Gassmann, F., 1951, Über die elastizität poröser medien: Vierteljahrsschrift der Natur- forschenden Gesellschaft in Zurich, **96**, 1–23.

Gaus, I., M. Azaroual, and I. Czernichowski-Lauriol, 2005, Reactive transport modelling of the impact of CO_2 injection on the clayey cap rock at Sleipner (North Sea): Chemical Geology, **217**, 319–337, doi: 1016/j.chemgeo.2004.12.016.

Ghaderi, A., and M. Landrø, 2009, Estimation of thickness and velocity changes of injected carbon dioxide layers from prestack time-lapse seismic data: Geophysics, **74**, no. 2, O17–O28, doi: 10.1190/1.3054659.

Ghosh, R., M. K. Sen, and N. Vedanti, 2015, Quantitative interpretation of CO_2 plume from Sleipner (North Sea), using post-stack inversion and rock physics modeling: International Journal of Greenhouse Gas Control, **32**, 147–158, doi: 10.1016/j.ijggc.2014.11.002.

Golding, M., and H. Huppert, 2011, The effect of confining impermeable boundaries on gravity currents in a porous medium: Journal of Fluid Mechanics, **649**, 1–17, doi: 10.1017/S0022112009993223.

Halko, N., P.-G. Martinsson, and J. Tropp, 2011, Finding structure with randomness: Probabilistic algorithms for constructing approximate matrix decompositions: SIAM Review, **53**, 217–288, doi: 10.1137/090771806.

Hashin, Z., and S. Shtrikman, 1963, A variational approach to the elastic behavior of multiphase materials: Journal of the Mechanics and Physics of Solids, **11**, 127–140, doi: 10.1016/0022-5096(63)90060-7.

Hoversten, G. M., F. Cassassuce, E. Gasperikova, G. A. Newman, J. Chen, Y. Rubin, Z. Hou, and D. Vasco, 2006, Direct reservoir parameter estimation using joint inversion of marine seismic AVA and CSEM data: Geophysics, **71**, no. 3, C1–C13, doi: 10.1190/1.2194510.

Hustedt, B., S. Operto, and J. Virieux, 2004, Mixed-grid and staggered-grid finite difference methods for frequency domain acoustic wave modelling: Geophysical Journal International, **157**, 1269–1296, doi: 10.1111/j.1365-246X.2004.02289.x.

Johnson, D., 2001, Theory of frequency dependent acoustics in patchy-saturated porous media: Journal of Acoustical Society of America, **110**, 682–694, doi: 10.1121/1.1381021.

Johnson, D., J. Koplik, and R. Dashen, 1987, Theory of dynamic permeability and tortuosity in fluid-saturated porous media: Journal of Fluid Mechanics, **176**, 379–402, doi: 10.1017/S0022112087000727.

Liang, L., A. Abubakar, and T. M. Habashy, 2016, Reservoir property mapping and monitoring from joint inversion of time-lapse seismic, electromagnetic, and production data: Geophysics, **81**, no. 5, ID73–ID84, doi: 10.1190/geo2015-0620.1.

Lindeberg, E., 2013, Calculation of thermodynamic properties of CO_2, CH_4, H_2O and their mixtures also including salt with the Excel macro CO_2 thermodynamics: SINTEF Report.

Mavko, G., T. Mukerji, and J. Dvorkin, 2009, The rocks physics handbook, tools for seismic analysis in porous media, 2nd ed.: Cambridge University Press.

Métivier, L., R. Brossier, J. Virieux, and S. Operto, 2013, Full waveform inversion and the truncated Newton method: SIAM Journal on Scientific Computing, **35**, B401–B437, doi: 10.1137/120877854.

Mohapatra, A., C. S. Rai, C. H. Sondergeld, and T. Richards, 2012, Laboratory study of velocity variations during CO_2 flooding in Tuscaloosa sandstone: Presented at the SPE Annual Technical Conference and Exhibition.

Muller, T., B. Gurevich, and M. Lebedev, 2010, Seismic wave attenuation and dispersion resulting from wave-induced flow in porous rocks: A review: Geophysics, **75**, no. 5, 75A147–75A164, doi: 10.1190/1.3463417.

Operto, S., Y. Gholami, V. Prieux, A. Ribodetti, R. Brossier, L. Metivier, and J. Virieux, 2013, A guided tout of multi-parameter full-waveform inversion with multicomponent data: From theory to practice: The Leading Edge, **32**, 1040–1054, doi: 10.1190/tle32091040.1.

Park, J., M. Fawad, I. Viken, E. Aker, and T. I. Bjørnarå, 2013, CSEM sensitivity study for Sleipner CO_2-injection monitoring: Energy Procedia, **37**, 4199–4206, doi: 10.1016/j.egypro.2013.06.322.

Pride, S., 2005, Relationships between seismic and hydrological properties, *in* Hydrogeophysics: Springer, Water Science and Technology Library, 253–284.

Pride, S., J. Berryman, and J. Harris, 2004, Seismic attenuation due to wave-induced flow: Journal of Geophysical Research, **109**, 1–19, doi: 10.1029/2003JB002639.

Queißer, M., and S. C. Singh, 2013, Full waveform inversion in the time lapse mode applied to CO_2 storage at Sleipner: Geophysical Prospecting, **61**, 537–555, doi: 10.1111/j.1365-2478.2012.01072.x.

Raknes, E. B., B. Arntsen, and W. Weibull, 2015, Three-dimensional elastic full waveform inversion using seismic data from the Sleipner area: Geophysical Journal International, **202**, 1877–1894, doi: 10.1093/gji/ggv258.

Ravaut, C., S. Operto, L. Improta, J. Virieux, A. Herrero, and P. dell'Aversana, 2004, Multi-scale imaging of complex structures from multi-fold wide-aperture seismic data by frequency-domain full-wavefield inversions: Application to a thrust belt: Geophysical Journal International, **159**, 1032–1056, doi: 10.1111/j.1365-246X.2004.02442.x.

Ravazzoli, C. L., and J. L. Gómez, 2014, Seismic reflectivity in carbon dioxide accumulations: A review, carbon sequestration and valorization: InTech, 343–360.

Reuss, A., 1929, Berechnung der fliebgrenze von mischkristallen auf grund der plastiz-itatsbedingung fur einkristalle: Zeitschrift fiir Angewandte Mathematik und Mechanik/Journal of Applied Mathematics and Mechanics, **9**, 49–58, doi: 10.1002/(ISSN)1521-4001.

Romdhane, A., and E. Querendez, 2014, CO_2 characterization at the Sleipner field with full waveform inversion: Application to synthetic and real data: Energy Procedia, **63**, 4358–4365, doi: 10.1016/j.egypro.2014.11.470.

Rubino, J. G., D. R. Velis, and M. D. Sacchi, 2011, Numerical analysis of wave-induced fluid flow effects on seismic data: Application to monitoring of CO_2 storage at the Sleipner field: Journal of Geophysical Research, **116**, doi: 10.1029/2010JB007997.

Sambridge, M. S., 1999a, Geophysical inversion with a neighbourhood algorithm. I. Searching a parameter space: Geophysical Journal International, **138**, 479–494, doi: 10.1046/j.1365-246X.1999.00876.x.

Sambridge, M. S., 1999b, Geophysical inversion with a neighbourhood algorithm. II. Appraising the ensemble:

Geophysical Journal International, **138**, 727–746, doi: 10
.1046/j.1365-246x.1999.00900.x.

Span, R., and W. Wagner, 1996, A new equation of state for carbon dioxide covering the fluid region from the triple-point temperature to 1100 K at pressures up to 800 MPa: Journal of Physical and Chemical Reference Data, **25**, 1509–1596, doi: 1063/1.555991.

Tarantola, A., 2005, Inverse problem theory and methods for model parameter estimation: SIAM.

Teja, A., and P. Rice, 1981, Generalized corresponding states method for viscosities of liquid mixtures: Industrial and Engineering Chemistry Fundamentals, **20**, 77–81, doi: 10.1021/i100001a015.

Vernik, L., D. Fisher, and S. Bahret, 2002, Estimation of net-to-gross from P and S impedance in deepwater turbidites: The Leading Edge, **21**, 380–387, doi: 1190/1.1471602.

Voigt, W., 1889, Uber die beziehung zwischen den beiden elastizitatkonstanten isotroper körper: Annalen der Physik, **274**, 573–587, doi: 10.1002/(ISSN)1521-3889.

White, J. C., G. A. Williams, and R. A. Chadwick, 2013, Thin layer detectability in a growing CO_2 plume: Testing the limits of time-lapse seismic resolution: Energy Procedia, **37**, 4356–4365, doi: 10.1016/j.egypro.2013.06.338.

White, J. E., 1975, Computed seismic speeds and attenuation in rocks with partial gas saturation: Geophysics, **40**, 224–232, doi: 10.1190/1.1440520.

Williams, G., and A. Chadwick, 2012, Quantitative seismic analysis of a thin layer of CO_2 in the Sleipner injection plume: Geophysics, **77**, no. 6, R245–R256, doi: 10.1190/geo2011-0449.1.

Zhu, H., S. Li, S. Fomel, G. Stadler, and O. Ghattas, 2016, A Bayesian approach to estimate uncertainty for full-waveform inversion using a priori information from depth migration: Geophysics, **81**, no. 5, R307–R323, doi: 10.1190/geo2015-0641.1.

Zweigel, P., R. Arts, A. E. Lothe, and E. B. Lindeberg, 2004, Reservoir geology of the Utsira Formation at the first industrial-scale underground CO_2 storage site (Sleipner area, North Sea): Geological Society, London, Special Publications 233, 165–180.

Bastien Dupuy received a degree (2008) in geotechnics and applied geophysics from the Joseph Fourier University (Grenoble, France) and a Ph.D. (2011) in geophysics from the Joseph Fourier University. He is currently a research scientist at SINTEF Petroleum Research (Trondheim, Norway). His research interests include seismic modeling in complex media, quantitative seismic imaging, and rock physics.

Anouar Romdhane received a Ph.D. (2010) in geophysics from the Pierre and Marie Curie University, Paris. He is a research scientist at SINTEF Petroleum Research in Trondheim, Norway. His research interests include CO_2 monitoring, seismic and electromagnetic modeling, full-waveform inversion, uncertainty evaluation, and rock physics analysis.

Peder Eliasson received an M.S. (2003) in physics and a Ph.D. (2008) in physics. Since 2009, he has been working as a research scientist and research manager in the geophysics group of SINTEF Petroleum Research. His research interests include finite-difference geophysical methods for modeling and inversion of seismic and electromagnetic data, joint inversion, uncertainty quantification in monitoring, and monitoring of CO_2 storage in general.

Verónica A. Torres received a bachelor's degree (2010) in geophysical engineering from the Central University of Venezuela. She joined IHS as a technical support of seismic interpretation software Kingdom Suit in 2011. She started working for Petroleum Geo-Services, Mexico, as seismic interpreter and geophysicist within the depth imaging team in 2012. She worked in 4D, 3D seismic land projects in the Gulf of Mexico with the aim of improving the subsalt seismic imaging. She is currently finishing her master's degree in petroleum geophysics from the Norwegian University of Sciences and Technology (NTNU), whose specialization is related to quantitative seismic interpretation, rock physics modeling, and seismic wave propagation in poroelastic medium.